A Chandra X-ray Survey of Ejecta in the Cassiopeia A Supernova Remnant

Una Hwang[1] & J. Martin Laming[2]

ABSTRACT

We present a survey of the X-ray emitting ejecta in the Cassiopeia A supernova remnant based on an extensive analysis of over 6000 spectral regions extracted on 2.5-10″ angular scales using the Chandra 1 Ms observation. We interpret these results in the context of hydrodynamical models for the evolution of the remnant. The distributions of fitted temperature and ionization age are highly peaked and suggest that the ejecta were subjected to multiple secondary shocks. Based on the fitted emission measure and element abundances, and an estimate of the emitting volume, we derive masses for the X-ray emitting ejecta as well as showing the distribution of the mass of various elements over the remnant. The total shocked Fe mass appears to be roughly 0.14 M⊙, which accounts for nearly all of the mass expected in Fe ejecta. We find two populations of Fe ejecta, that associated with normal Si-burning and that associated with α-rich freeze-out, with a mass ratio of approximately 2:1. Surprisingly, essentially all of this Fe (both components) is well outside the central regions of the SNR, presumably having been ejected by hydrodynamic instabilities during the explosion. We discuss this, and its implications for the neutron star kick.

Subject headings: hydrodynamics – ISM: individual (Cassiopeia A) – supernova remnants – X-rays: ISM

---

[1]Goddard Space Flight Center and Johns Hopkins University

Una.Hwang-1@gsfc.nasa.gov

[2]Code 7674L, Naval Research Laboratory, Washington DC 20375

laming@nrl.navy.mil

1. Introduction

Theory and observations are merging toward consensus that core-collapse supernova explosions are intrinsically asymmetric, even if the progenitor had an initially symmetric configuration. Recent three-dimensional simulations show that strong dynamical interactions between the various burning shells can lead to large asymmetries in the progenitors, independent of the symmetry of the explosion (Arnett & Meakin 2011). Nor is the explosion itself likely to be spherical, with convective instabilities (e.g. Herant et al. 1992; Herant 1995) and instabilities at the accretion shock (e.g. Blondin et al. 2003; Foglizzo et al. 2007) all possibly acting to create asymmetries. It is further anticipated that such asymmetries may hold the key to the core-collapse explosion mechanism (e.g. Ott et al. 2008; Brandt et al. 2011). They will be manifested not only in the distributions of the ejecta mass and velocity, but also in the recoil of the nascent neutron star, which is observed with measured space velocities of up to 1000-1500 km/s (Arzoumanian et al. 2002; Hobbs et al. 2005; Faucher-Giguère & Kaspi 2006). Simulations show that a neutron star kick that has a purely hydrodynamic origin can balance the total momentum of the anisotropic component, and is expected in the direction opposite the fastest shock expansion (Wongwathanarat et al. 2010; Scheck et al. 2004).

Observations of core-collapse supernovae indicate a significant degree of explosion asymmetry via measurements such as time-dependent polarization changes or Doppler velocities (Mazzali et al. 2006; Leonard et al. 2006), but explosion asymmetries are also revealed in sufficiently young supernova remnants (SNRs) through their shock-heated ejecta. The most detailed view so far available of the ejecta in a young core-collapse SNR is provided by Cassiopeia A, which at 330 years is the penultimate of the known Galactic supernova remnants. Its reverse shock has already progressed deeply into the explosively produced nucleosynthesis products, aided by the strong presupernova mass loss incurred by its progenitor through the likely action of a binary companion (Young et al. 2006).

That Cas A was produced by an asymmetric explosion is by now well-established, and most recently by light echo observations which sample the explosion hundreds of years after the fact in different directions. These show variations in the ejecta velocities of $\sim$ 4000 km/s (Rest et al. 2010). Chandra X-ray observations have also played an important role in revealing the complexity of Cas A's X-ray emitting ejecta. The X-ray emitting Si ejecta show a bipolar structure with jet-like features (Hwang et al. 2004; Vink et al. 2004; Laming et al. 2006) similar to that seen in optical (Fesen 2001, and references therein) and infrared emission (Hines et al. 2004). The X-ray ejecta spectra reveal the imprint of roughly a factor of two asymmetries in the deposition of explosion energy around the remnant (Laming & Hwang 2003), similar to the distribution of kinetic energies and positions of fast moving

optical knots (Hammell & Fesen 2008). Early Chandra observations identified regions dominated by emission from Fe ejecta well outside the projected location of Si emission that were proposed to be sites of overturn between the nucleosynthesis layers (Hughes et al. 2000). This conclusion is apparently supported by the X-ray Doppler measurements showing higher velocities of Fe compared to Si (Willingale et al. 2002). More recently, the dynamical structure of the ejecta has been inferred in remarkable detail by the multi-wavelength (X-ray, optical, infrared) Doppler-shift maps compiled by DeLaney et al. (2010). These show the inner ejecta to be unshocked and in a flattened distribution ([Si II]), outlying matter ([Ar II], [Ne II]) to be arranged in rings on a spherical surface, with outflows emerging out of the surface of the remnant (Fe ejecta, jet, and counterjet). Their detailed analysis shows that the outflows of X-ray emitting Fe ejecta are not material mixed outwards from overturning of the ejecta layers, but rather, material that has pushed through the overlying ejecta and are now encircled by rings of material from outlying nucleosynthesis layers.

Large-scale studies of the X-ray emission in Cas A have already been undertaken by Stage et al. (2006) and Helder & Vink (2008), but these focus on the properties of the nonthermal emission. The most comprehensive accounting of the X-ray emitting ejecta in Cas A to date was carried out by Willingale et al. (2003), who used XMM-Newton CCD observations to examine 225 regions of fixed $20''$ size across Cas A (Willingale et al. 2002). They fitted a two-component thermal model throughout to represent hot shocked circumstellar material and cooler shocked ejecta and inferred a total ejecta mass of 2.2 $M_\odot$. They interpret the Fe K emission as forming a bipolar double cone that is associated with ejecta bullets that have broken beyond the forward shock.

A detailed accounting of the X-ray emitting ejecta on fine angular scales was one of the primary goals of a 1 Ms Chandra observation of Cassiopeia A that was obtained in 2004, and is the subject of this paper. Our spectral survey includes over 6000 spectral regions extracted on 2.5-$10''$ angular scales. It is distinguished from previous Chandra studies of the ejecta in Cas A, which have relied either on spectral imaging or the detailed spectral analysis of a relatively small number of regions. We are able to cover a larger area of the remnant with much higher sensitivity and angular resolution than was available to Willingale et al. (2002). In particular, we are able to show the distribution of the X-ray emitting Fe ejecta in detail. The Fe ejecta, being produced just outside the collapsing core of the supernova, provide valuable clues to understand important details of the explosion, including the recoil of the ejecta with the neutron star.

We interpret the spectra in the context of the hydrodynamical models applied by us previously to Cas A (Laming & Hwang 2003; Hwang & Laming 2003; Laming et al. 2006; Hwang & Laming 2009). Cas A particularly lends itself to quantitative analysis by virtue of

its well-constrained age (Thorstensen et al. 2001; Fesen et al. 2006) and distance (Reed et al. 1995). Recent one-dimensional hydrodynamical models for the interaction of the remnant with a circumstellar wind medium indicate that the reverse shock in Cas A has already interacted with a significant fraction of the ejecta (Chevalier & Oishi 2003). Laming & Hwang (2003) apply their models directly to Chandra X-ray spectra, and also infer that there is very little of the unshocked ejecta remaining. Thus a large fraction of the ejecta in Cas A are accessible to X-ray observations, the exceptions being the small amount of ejecta that have not yet been shocked, any ejecta that might have been subject to rapid cooling by thermal instability, and ejecta of very high density that have been shocked to lower temperatures and thus emit at longer wavelengths as optical knots (e.g. Fesen 2001).

The organization of the paper is as follows: Section 2 begins by giving an overview of the analysis procedure, with explanations as to the spectral grid and background, and most importantly how the spectra were organized according to the fitting model required. We then proceed to discuss the results, from maps for the remnant as a whole, to a few observations about properties of the forward shock-dominated regions, and then the ejecta. Section 3 discusses issues concerning the models and the refinements that have been made for this work compared to previous work. Section 4 then presents the results of the mass calculation and issues connected to it, such as the presence of unshocked ejecta and implications for the neutron star kick.

2. Analysis Procedure

We use the 1 Ms Advanced CCD Imaging Spectrometer (ACIS) observation obtained by the Chandra X-ray Observatory in February and May 2004 (one of the first Chandra VLP, or Very Long Project, observations). This observation is described by Hwang et al. (2004). Its most salient features are that it was obtained in nine observation segments (OBSIDS) and in GRADED mode, wherein the CCD detection events are characterized onboard the spacecraft before telemetry. It was necessary to use GRADED mode to reduce the telemetry load, due to the high source count rate (the observation accumulated some 280 million photon events in 980 ks). The main disadvantage of using GRADED mode is that detailed corrections of detector problems such as pulse pile up are not possible. The data were processed with CALDB Version 3.2.2.

In this section, we outline the analysis procedure, which includes definition of the spectral grid, considerations for the subtraction of the background, the classification of forward shock and ejecta-dominated spectra, the selection of appropriate spectral models, and the results of the fitting.

2.1. Spectral Grid

To carry out our spectral survey of the ejecta in Cas A, we define a grid of 10″ boxes across the entire supernova remnant (SNR), optionally subdividing by factors of two down to 2.5″ depending on the number of counts. The regions are thus square or rectangular with sides of length 2.5, 5, or 10″. We excluded the regions dominated by the central compact object, and a few other regions with low numbers of counts. This gave us 6202 spectra for analysis. Although this is a very large number, the data would have readily allowed at least a factor of two finer grid sizes down to nearly the Chandra angular resolution in some regions. This being the first attempt at an analysis of the complex thermal emission on such a fine angular scale, we tried to keep the number of grid regions relatively tractable.

Each spectrum was then extracted individually from all nine OBSIDS comprising the Ms observation, and the corresponding individual photon redistribution matrices and effective area files computed. The individual spectra were then added, and the individual response files weighted and added, to obtain the final spectral and response files for each grid region. The pulse-height spectra were further binned to yield a minimum of 25 counts per bin to apply Gaussian statistics.

The filamentary and knotty characteristics of Cas A's X-ray emission, its high surface brightness, and the excellence of the Chandra mirrors, result in pulse pile-up at the brightest ejecta knots. Pulse pile-up can produce spurious line features, for example, with energies that correspond roughly to the summed energy of the Si and/or S He α blends that are so prominent in Cas A. Pile-up of continuum photons will also skew the spectral shape to yield higher fitted temperatures.

A detailed correction for pulse pile-up cannot be performed for these GRADED mode data, and we made no attempt to account for these effects for the thousands of spectra examined here. We can, however, estimate qualitatively the number of our spectra for which pile-up is a significant problem. For the *vpshock* fits described later (in section 2.3), we consider the distribution of the fitted temperature against the counts per pixel for each spectrum. The average fitted temperature shows a clear trend of increasing for spectra with more than about 6000 counts/pixel in 980 ks[3]. For the 25 regions with the highest count/pixel ratios ($>$ 6000 counts/pixel), the average fitted temperature is 2.25 keV, which is significantly higher than the average of 1.7 keV for the remaining spectra. Inspection of

[3]The count/pixel cut-off we discuss here is of course specific for this particular observation. For reference, the brightest pixels contain on the order of 16000 counts, corresponding to a count rate of 0.05 counts per 3.24 s frame. This corresponds roughly to pileup fractions of less than a few percent according to the Chandra Proposers' Observatory Guide.

these spectra show the problems in fitting the line emission described above; these problems are not apparent for lower count-rate spectra. Since the pile-up occurs noticeably in only a limited number of regions ($\sim$25), we expect that its uncorrected effect on the total mass is not large.

2.2. Background

The off-source regions outside the SNR show a line-rich spectrum similar to that of the SNR itself. The background is thus dominated by the bright source spectrum due to scattering by intervening dust, the CCD readout, and to a lesser extent, the wings of the mirror point spread function. Dust scattering has been shown to be significant for Cas A based on ROSAT and Einstein observations by Predehl & Schmitt (1995) and Mauche & Gorenstein (1989).

Since the source spectrum, and hence the background, varies both in form and brightness around the remnant, we extract 16 separate background spectra by subdividing a $0.4'$ thick, $\sim 3.5'$ radius circular shell surrounding the remnant so that each segment covers roughly 20 degrees in azimuth. We then assign a background spectrum for each source spectrum based on the source region's azimuthal position angle. Where the source extends beyond the background extraction radius, near the northeast "jet" and its southwest counterpart, we use the sum of the two nearest background regions to either side.

We choose to subtract the background from the source spectrum rather than to fit a model to each background spectrum. A model for the background would have to include a thermal component for the scattered source spectrum, whose normalization would inevitably be difficult to constrain. The normalization for the particle background component is well-constrained by the spectrum at high energies, but the effect of scaling the scattered thermal background in the same way as the particle background is similar to simply subtracting the total background.

Simple subtraction of the off-source background means that the background is generally underestimated, and by different amounts depending on the photon energy and the dominant scattering process. The precise determination of the background is thus a sophisticated problem that is beyond the scope of our study. The ejecta survey which is the focus of our efforts will be less sensitive to the precise background subtraction because most of the ejecta regions are bright, with strong line emission; the subtleties of the background subtraction are less important here than for inferences about the origin of weak lines.

2.3. Spectral Classification

2.3.1. Spectral Map

To provide a consistent spectral characterization of the entire remnant, we fit to every spectrum in our grid a single-component plane-parallel shock model with variable element abundances (XSPEC model *vpshock*; Borkowski et al. 2001) modified by interstellar absorption (XSPEC model *wabs*; Morrison & McCammon, 1983). The *vpshock* model incorporates ionization ages from zero up to a fitted maximum value. In previous work (Laming & Hwang 2003; Hwang & Laming 2003), we had used simple nonequilibrium ionization (NEI) models characterized by a single temperature and ionization age, but there the extraction regions were generally as small as $3''$ and the exposure time only 50 ks. We find that for the much longer exposure time of these data, and the sometimes larger extraction regions, such models are no longer acceptable. Because most of the regions have ejecta-dominated spectra, we have not included any elements lighter than O in the model, taking O to be the primary source of the continuum in the manner of Vink et al. (1996), Laming & Hwang (2003) and Hwang & Laming (2003). The abundances of elements heavier than O are generally varied (with Ni linked to Fe, Ca to Ar, and sometimes Ar to S), while O is held fixed at the solar value, using the solar abundances of Anders & Grevesse (1989). The redshift is allowed to vary to either positive or negative values, given that the ejecta in Cas A have significant bulk motions (e.g., Markert et al. 1983; Willingale et al. 2002), and is generally driven by the Fe L emission and the strong Si blend. Given that there may be calibration problems near Si (see the discussion in DeLaney et al. 2010), we consider the fitting of the redshift more as an aid to achieving good fits rather than a reliable measure of the actual line-of-sight velocity. The fitted redshift does, however, reproduce the gross features of the bulk motion as measured by other means. A Gaussian smoothing scale for the spectrum was also fitted, given that the observed strong spectral lines are generally broad.

While we do not present errors for the fitted parameters here, these were computed for key parameters. We have found that this is a necessary step to optimize finding the true minima: the χ^2 terrain is generally rather rugged for these fits. The redshift and ionization age in particular are prone to settle at secondary minima, as might be expected, considering that these parameters both have a strong effect on the energies of the strong line features.

Here we note some of the general features of these results based on images shown in Figure 1, where fitted model parameters such as temperature, ionization age, and various element abundances are shown for each spectral region, and histograms and a scatter plot for the fitted temperatures and ionization ages shown in Figure 2. The column density increases systematically to the west by about a factor of 2 or more and reaches a maximum

at the western extremity of the remnant. This is entirely consistent with previous work (Keohane et al. 1996; Willingale et al. 2002). There are also smaller regions in the center with significant localized column density enhancements. The temperature distribution has two peaks, seen most clearly in the histogram in Figure 2, with the lower peak associated with ejecta-dominated regions and the higher with FS-dominated regions. The ionization age, by contrast, is remarkably narrowly distributed overall, though coherent regions with high ionization ages can be identified on the map in Figure 1. In the western half of the remnant, these high ionization regions appear to be associated with the FS. The highest ionization ages are found in the east, however, and there they are clearly associated with Fe-enriched ejecta, as is apparent from comparing the ionization age and Fe abundance maps shown in Figure 1.

We will focus our attention primarily on the abundance maps for Fe and Si, although such maps are also shown for all the elements for which we fitted the abundances. The maps for S and Ar are on the whole similar to that of Si. The abundance maps for Si and Fe are distinctly different, but both feature three main lobes of ejecta located north, east, and west. The Si is also extended to the northeast along the northeast ejecta "jet", while Fe is particularly distinct in the eastern region compared to the Si, and shows its highest enhancement in the outermost parts of this region. In general, the abundance maps we obtain are strongly reminiscent of the corresponding line images shown by Hwang, Holt, & Petre (2000) and Hwang et al. (2004), and also resemble the abundance maps obtained by Willingale et al. (2002). Those authors have previously noted that the line emission and element abundance patterns for Si, S, Ar, and Ca in Cas A are similar to each other.

The Ne and Mg maps show a distinct character in that they do not show any prominent morphological characteristics aside from a brightening at the western end of the remnant. One must be cautious to interpret those results, however, as the the line emissions of Ne and Mg fall in complicated parts of the spectrum, and the abundances of these elements may be correlated in complicated ways with parameters such as the ionization age, which shows similar distribution patterns in the west, and the column density, which is very high in that region. It is clear, however, that Ne and Mg both show a strikingly different morphology to Si, S, and Ar, or to Fe, and are much more similar to each other than to any of the other elements.

2.3.2. Forward Shocked Regions

Broadly speaking, the distinctions between ejecta- and FS-dominated regions in Cas A are readily apparent, with differences in temperature, ionization age, and element abun-

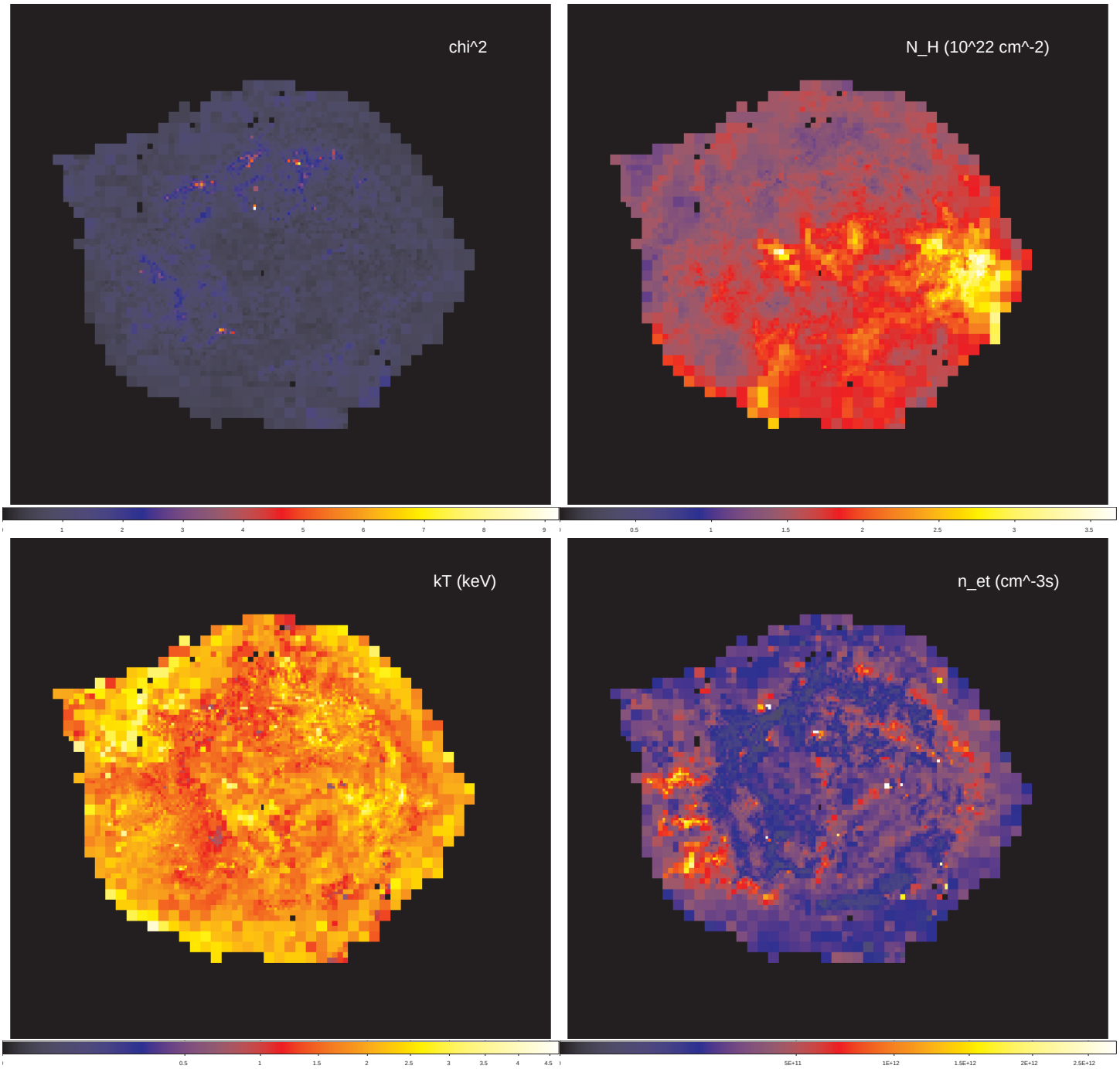
chi^2
1
2
3
4
5
6
7
8
9
N_H (10^22 cm^-2)
0.5
1
1.5
2
2.5
3
3.5
kT (keV)
0.5
1
1.5
2
2.5
3
3.5
4
4.5
n_et (cm^-3s)
5E+11
1E+12
1.5E+12
2E+12
2.5E+12

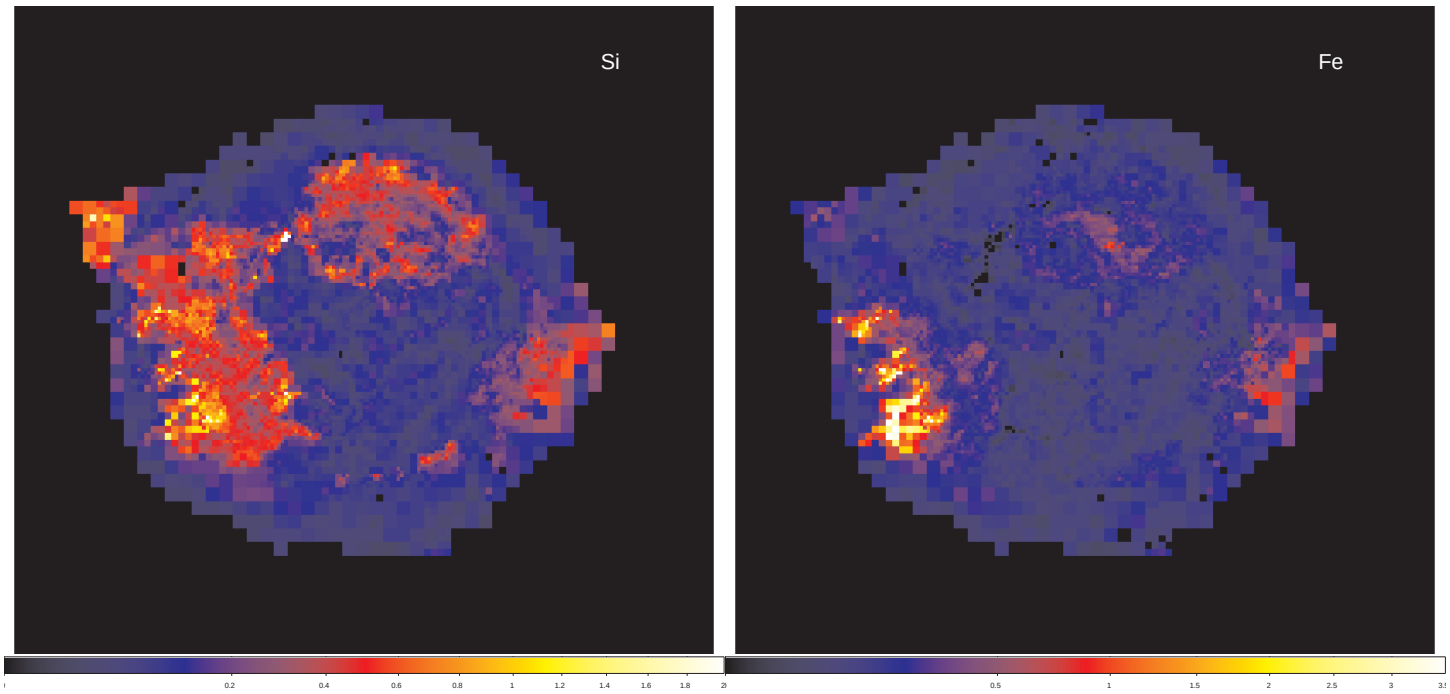

Fig. 1.— Partial set of fitted parameters for the single *vpshock* model fits. Top row: Maps of χ^2 per degree of freedom (left), and of fitted column density N_H in 10^{21} cm^2 (right). Middle row: Maps of temperature kT in keV and ionization age $n_e t$ in cm^{-3}s (sqrt scale). Bottom row: Maps of fitted Si and Fe element abundances, relative to the solar values of Anders & Grevesse (1989) by number, both on sqrt intensity scale, truncated at the high end.

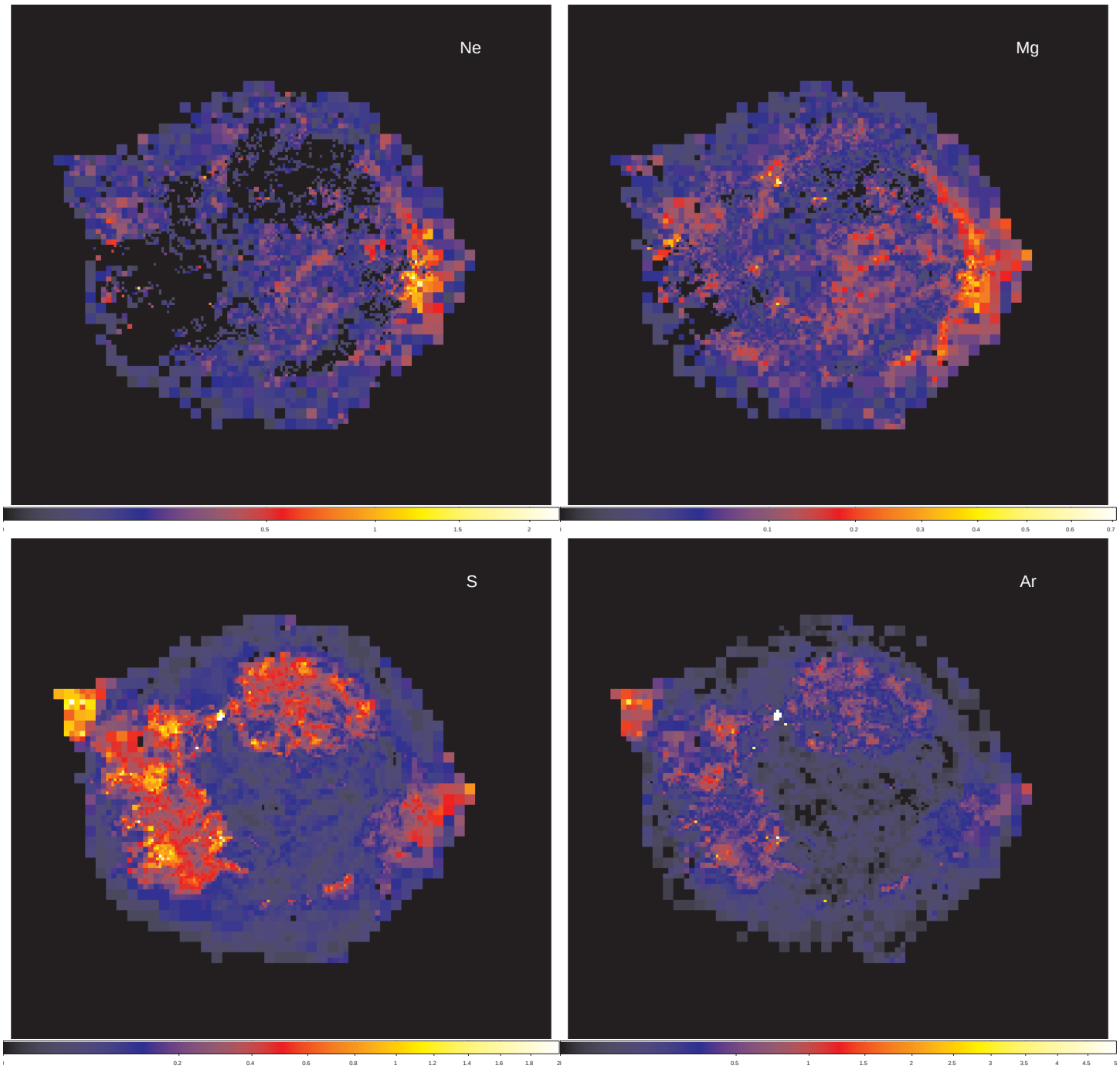

Fig. 1.— Fitted abundances of the remaining elements, Ne, Mg, S, Ar. The intensities are square-root scale and truncated at the high end for S and Ar.

dances. To carry out a survey of the ejecta mass, however, we must either model both the ejecta and CSM components for each spectrum or else identify the specific regions where the reverse-shocked ejecta make the dominant contribution to the emission. Given the scope of the spectral analysis, we have adopted the latter approach. Multi-component fits can be difficult to constrain reliably, particularly if one of the components is relatively weak, and thus would require more individual attention than is feasible for a sample of thousands. Consequently, our next aim is to identify and eliminate regions whose spectra can be completely associated with the forward shock.

We evaluate the presence of thermal emission associated with the forward shock by fitting a second set of plane-parallel shock models to every spectrum, but this time with element abundances appropriate for the CSM. The optically emitting quasi-stationary flocculi (QSFs) in Cas A are understood to be circumstellar mass loss from the progenitor, but abundance measurements for QSFs are limited to a small number of knots. These show an order of magnitude enhancement of N and sometimes also of He (Chevalier & Kirshner 1978). Theoretical calculations for the presupernova composition are also given by Arnett (1996), where the models allow the elements H, He, and N, all apparently present in Cas A, to exist simultaneously at a narrow temperature range near log T (10^9 K) = 1.5 (their Figure 7.6). At that temperature the abundance of He is 3 times the solar value of H by number, and that of N about 15 times the solar value. As these abundances for He and N are broadly consistent with the observational measurements, we proceed to adopt them for our fits, along with solar values for the remaining elements, as representative CSM element abundances.

About 1209 regions gave reasonably good fitting results ($\chi^2 \leq 1.2$) with the *vpshock* model and these element abundances, and are thus assigned to the forward shock. They are distributed mainly in the remnant's outer rim and southwest interior, as would be expected based on the 4-6 keV X-ray continuum image that highlights the forward-shocked regions (Gotthelf et al. 2001). Their average temperature is 2.2 keV, and their ionization ages are rather narrowly distributed with an average value of 2×10^{11} cm^{-3}s. These values can be assessed in the context of the models of Laming & Hwang (2003), which give the current density of the CSM at the forward shock at about 1.5-2 cm^{-3}. Considering the r^{-2} dependence of the circumstellar density, the forward shock will have encountered much denser material in the past and the present-day ionization state of the forward shocked material is expected to be relatively advanced. The models give values of the ionization age in the 10^{11} cm^{-3} s range, approaching 10^{12} cm^{-3}s; they also indicate that gas is also rather hot, with temperatures from 2.5-4 keV. The average values of the temperature and ionization age that we find in our regions are close to the range predicted by the models, though the fitted spectra don't show as broad a range in ionization age as is expected.

To the forward-shock regions identified solely by the thermal emission model above, we must also add those that have a strong nonthermal contribution. To identify these, we devise a rough diagnostic for the smoothness of the X-ray spectrum. We bin each background-subtracted spectrum at each significant line feature and continuum interval (some of these cover only a narrow energy range), compute the ratio of counts for each major line feature relative to counts in an adjacent continuum bin, and take the sum of these ratios for all the line features. The distribution of this quantity has two overlapping peaks; we take the spectra associated with the lower peak (corresponding to weak lines in the spectrum) and perform further fits with a composite plane-parallel pshock plus power-law model. For a cutoff in $\chi^2 \leq 1.2$ for these fits, we associate 206 additional regions with the forward shock, giving a total of 1415 regions with spectra that are consistent with emission associated with the forward shock alone.

Figure 3 summarizes the distribution and spectral characteristics of the forward shock regions. Their locations echo the 4-6 keV continuum maps shown by Gotthelf et al. (2001) and Hwang et al. (2004). As already noted, their temperatures and most especially their ionization ages are rather narrowly distributed, more so than for the sample as a whole. From the Figure, the peaks in the distributions correspond roughly to kT = 2.2 keV and log (n_e t) = 11.25, or $n_e t = 1.8e11$ cm^{-3}s. These regions will not be considered further here as we focus our study on the ejecta. We will undertake a detailed consideration of the thermal emission associated with the forward shock in subsequent work.

2.4. Spectral Survey of the Ejecta and the Presence of Pure Fe

We associate with ejecta the remaining, more than 4000, regions that are inconsistent with forward shocked material. For these regions, the basic spectral model is the simple one-component plane-parallel shock that has already been presented and discussed. As noted above, we take the view that, for the ejecta sample as a whole, it is justifiable to assume sufficient ejecta dominance to neglect the forward shock component. Representative examples of all the various types of spectra seen in Cas A are shown in Figure 5.

For some ejecta regions, the one-component spectral model is clearly inadequate to describe the ejecta emission in that it fails to account for the Fe K blend. This has already been noted by Hwang & Laming (2009). While there may be significant deficiencies in the atomic data that are used for the thermal emission models, particularly in the nonequilibrium ionization case, these cannot explain so large an effect as we see. In some cases, a strong Fe K blend is completely unaccounted for by the model, which otherwise characterizes the spectrum well.

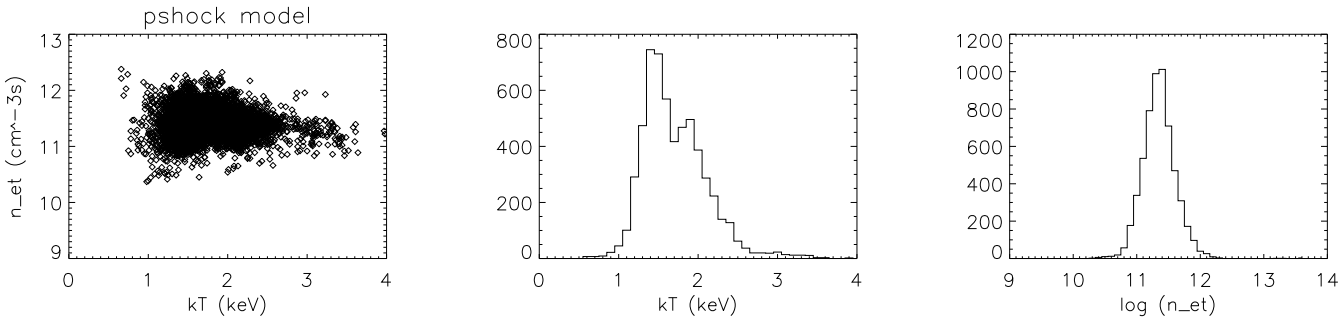

Fig. 2.— The distribution of temperature kT and ionization age $n_e t$ amongst the 6202 spectral regions fitted with *pshock* models (see Figure 1) : (left) two-dimensional distribution; (middle) histogram for temperature kT; (right) histogram for ionization age $n_e t$

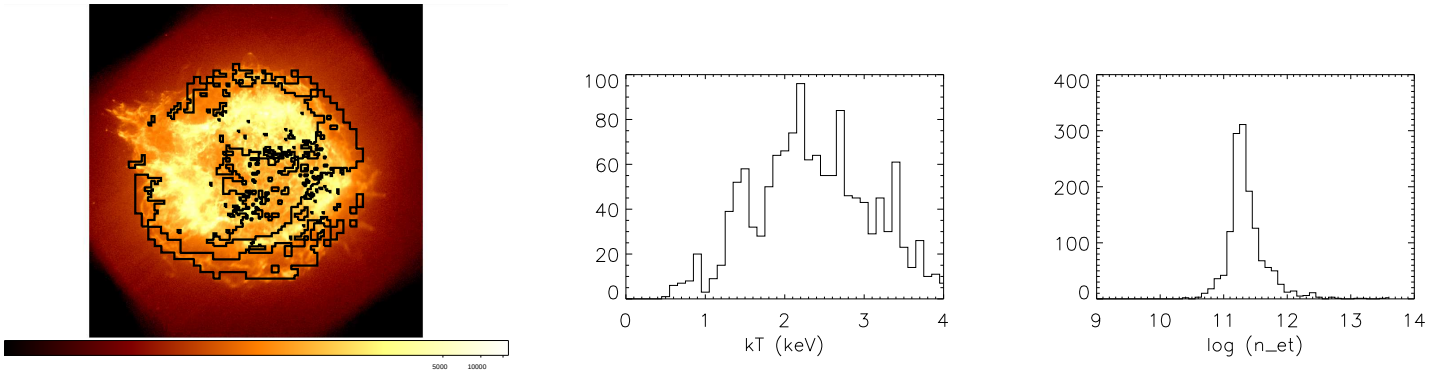

Fig. 3.— (left) Contours showing the 1415 regions that have been associated with the forward shock, and hence excluded for the ejecta mass calculation, based on the merged QSF and QSF+PL fits. For these forward shock regions is shown the distribution of fitted (middle) temperature kT (the scale is truncated above 10 keV), and (right) $\log_{10}$ ionization age $n_e t$.

Given the strong chemical inhomogeneities seen and expected in core-collapse supernova remnants, it is plausible that Fe-rich ejecta could be superposed along a given line of sight with ejecta of more normal composition, and that each would have distinct plasma conditions as well as abundances. Moreover, nucleosynthesis models predict the formation of nearly pure Fe ejecta by α-rich freeze-out during complete Si burning; this is in addition to ejecta composed of a range of elements from Si and Fe formed by incomplete Si-burning.

Hwang & Laming (2003) and Hwang et al. (2004) have reported the presence of highly enriched Fe ejecta in the southeastern region of Cas A, with one region particularly appearing to be a"pure Fe" cloud. We take another look at this region using the 1 Ms observation. Figure 4 shows a portion of the southeastern region of Cas A and the roughly $2.5''$ extraction region that we use for this cloud, which is smaller than that used by Hwang et al. 2003. The background is taken locally from the vicinity of the source region, and we compared results using three different background spectra. The background was modeled in this case, rather than subtracted, and the model included in the fit to the unbinned, unsubtracted source spectrum. The results for all three background subtractions gave fitted Fe/Si abundance ratios that are enhanced over the solar values by factors of 10-20 by number (or factors of 20-40 by mass). The right panel of Figure 4 shows the fit giving the highest Fe/Si ratio. Note the absence of recognizable emission from S or Ar, and the weakness of the Si emission; the emission lines at energies above 7 keV are of H-like Fe. These results demonstrate that it is possible to identify emission in Cas A that is plausibly associated with pure Fe.

For a subset of 700 regions with the strongest Fe line emission and the poorest fits in the Fe K band, we tested two options for the added component representing either shocked circumstellar medium or pure Fe and Ni ejecta. For the former, we take a plane-parallel shock with CSM abundances and the average temperature (2.2 keV) and ionization age (3×10^{11} cm^{-3}s) obtained for the forward shock regions, all as described above. For the latter, we found that a simple nonequilibrium ionization component, with a single value of the ionization age was sufficient, with the temperature fixed at 1.95 keV and the single value of the ionization age fixed at 8×10^{11} cm^{-3}s. These values are representative of the most enriched Fe ejecta spectra, such as those studied by Hwang & Laming (2003); the fits, however, are not strongly sensitive to the exact values used so long so long as they are of this approximate magnitude. We fix the parameters of the second component whenever possible because the limited spectral resolution makes it very difficult, even at these exceptionally high levels of signal-to-noise, to constrain both model components independently. As before, errors were calculated for key parameters to help ensure finding the true minimum in χ^2. Only one of these 700 ejecta+CSM fits gave $\chi^2 \leq 1$ in the 6-7 keV Fe K region, leading us to conclude that the presence of a forward shock component can not explain the strong Fe K emission. On the other hand, a majority of the *vpshock*+NEI fits did give acceptable

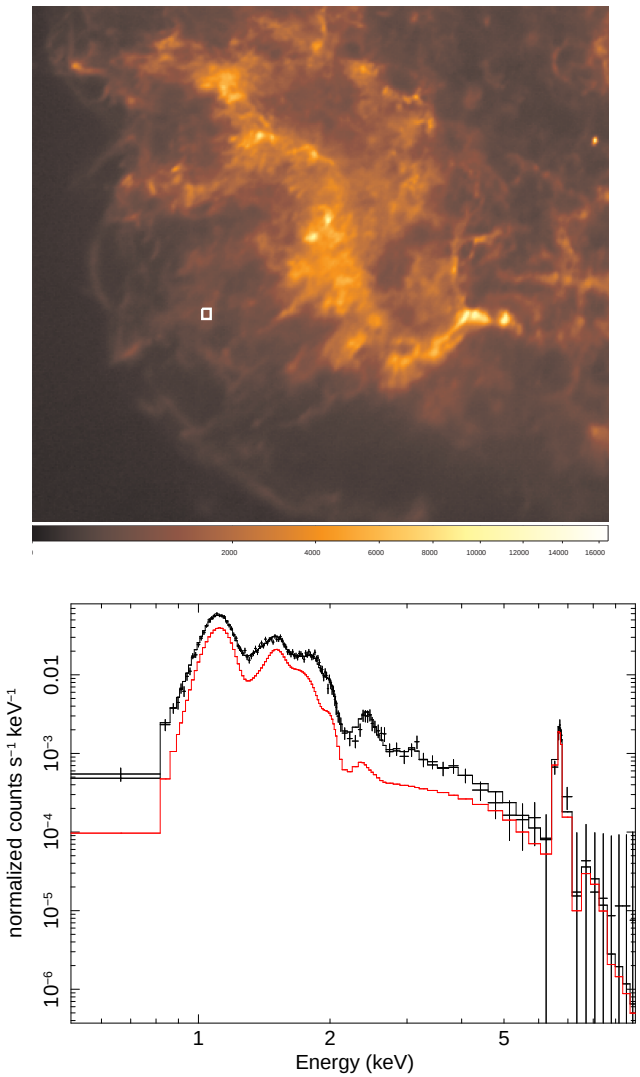

Fig. 4.— (Top) Southeast region of Cas A showing the extraction region used here for the pure Fe cloud of Hwang & Laming (2003). (Bottom) Fitted spectrum, in which the local background has been modelled rather than subtracted and the unbinned spectrum fitted using C-statistics. The spectrum is shown binned for clarity, with the black trace giving the total source plus background spectrum, and the red trace giving only the source spectrum.

χ^2 values in the 6-7 band, although the improvement was sometimes due to a better match to the continuum rather than the line emission. An example is shown in final two panel rows of Figure 5, where the same spectrum is shown with the original single-component *vpshock* fit, a two component *vpshock* fit for normal ejecta and shocked CSM, and finally a two ejecta-component fit where the added ejecta component is taken to be pure Fe (and Ni).

On a broader scale, we identify 3032 spectra where a composite ejecta model may be needed by selecting regions where the fitted Fe abundance for the basic single-component model was above 0.3 solar, and focus only on two component models with the usual *vpshock* ejecta component and a second (NEI) ejecta component corresponding to Fe. We evaluate using an f-test those regions where the improvement in fit from adding the second component was above a certain probability threshold. The calculation of the mass of various elements in the ejecta is discussed fully in Section 4. Here, we simply show in Figure 6, examples of the Fe mass distribution in the second, "pure" Fe component for probability cuts of 0.1, 0.01, and 0.001 for adding this component. The spatial distribution retains its main features regardless of the exact probability cut imposed.

3. SNR Models

In this section we provide an overview of our models for the evolution of Cas A. These are treated in a manner similar to that in Laming & Hwang (2003) and Hwang & Laming (2003), for expansion of the remnant into a circumstellar wind (density $\propto r^{-2}$), but with modifications that we discuss here.

3.1. Dynamics

We modify the models to accommodate SNR expansion into a stellar wind "bubble" as presented and discussed in Hwang & Laming (2009). The chief motivation involves the interpretation of infra-red light echoes associated with Cas A as reprocessed shock breakout radiation (Dwek & Arendt 2008). This radiation is concentrated in the UV-EUV spectral region, and would be strongly absorbed in photoionizing any intervening neutral gas, which presumably would be a relic of the red supergiant presupernova stellar wind. Most of this opacity would lie close to the progenitor, and so a small "bubble" in the circumstellar medium would allow the breakout radiation to escape and illuminate the surrounding dust.

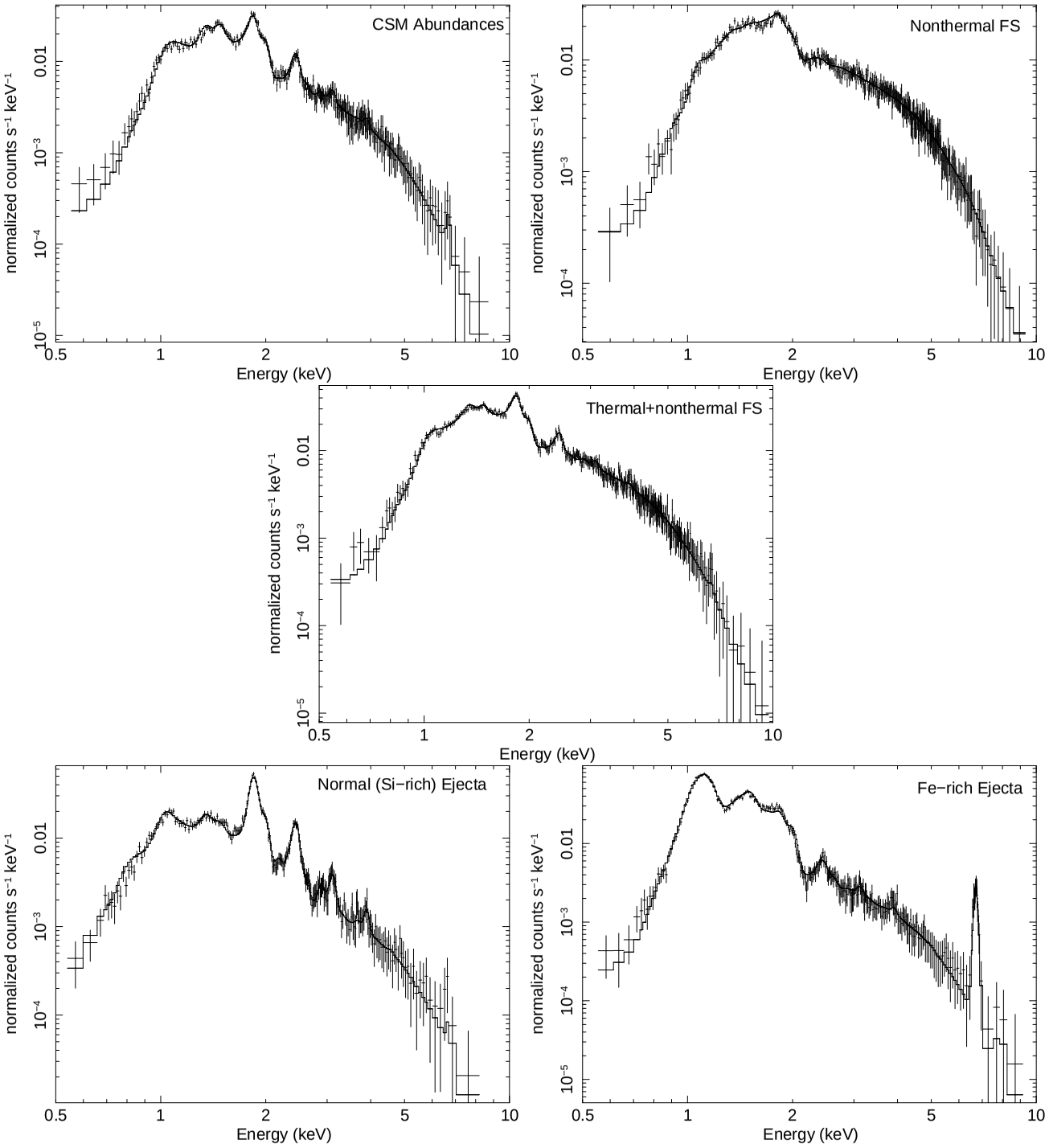
CSM Abundances
Nonthermal FS
Thermal+nonthermal FS
Normal (Si−rich) Ejecta
Fe−rich Ejecta
normalized counts s^{-1} keV^{-1}
Energy (keV)
0.5
1
2
5
10
0.01
10^{-3}
10^{-4}
10^{-5}

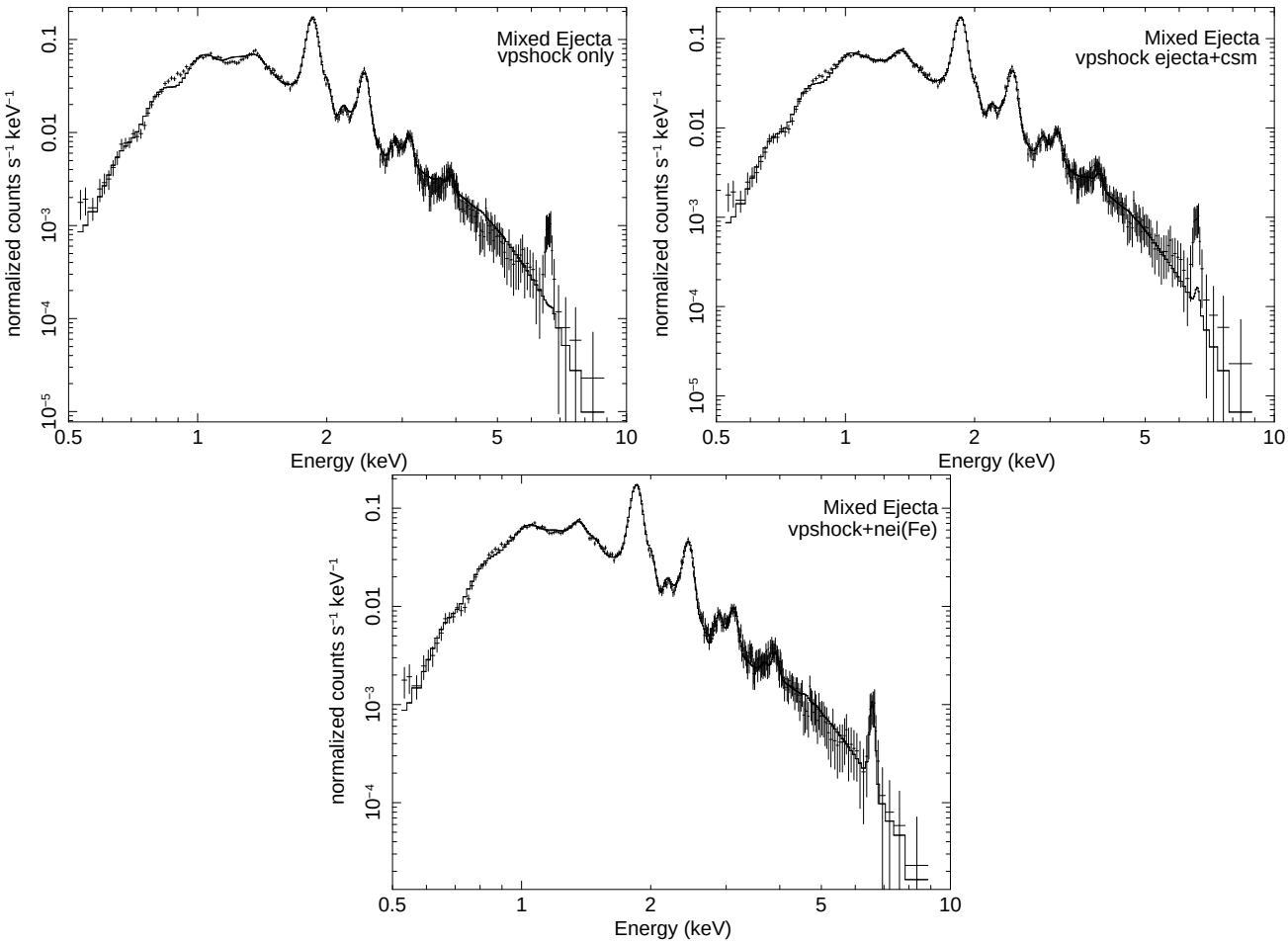

Fig. 5.— Sample spectra exemplifying typical spectral types seen in Cas A (first two rows) Spectra associated with the forward shock, showing various mixtures of thermal emission associated with shocked circumstellar medium and nonthermal emission. (third row) Typical "Si-dominated" and Fe-dominated ejecta spectra. (last two rows) For the same spectrum, a comparison of single-component *vpshock* ejecta models, ejecta plus shocked CSM models, and a model with two ejecta components corresponding to "normal" ejecta and "pure Fe" ejecta.

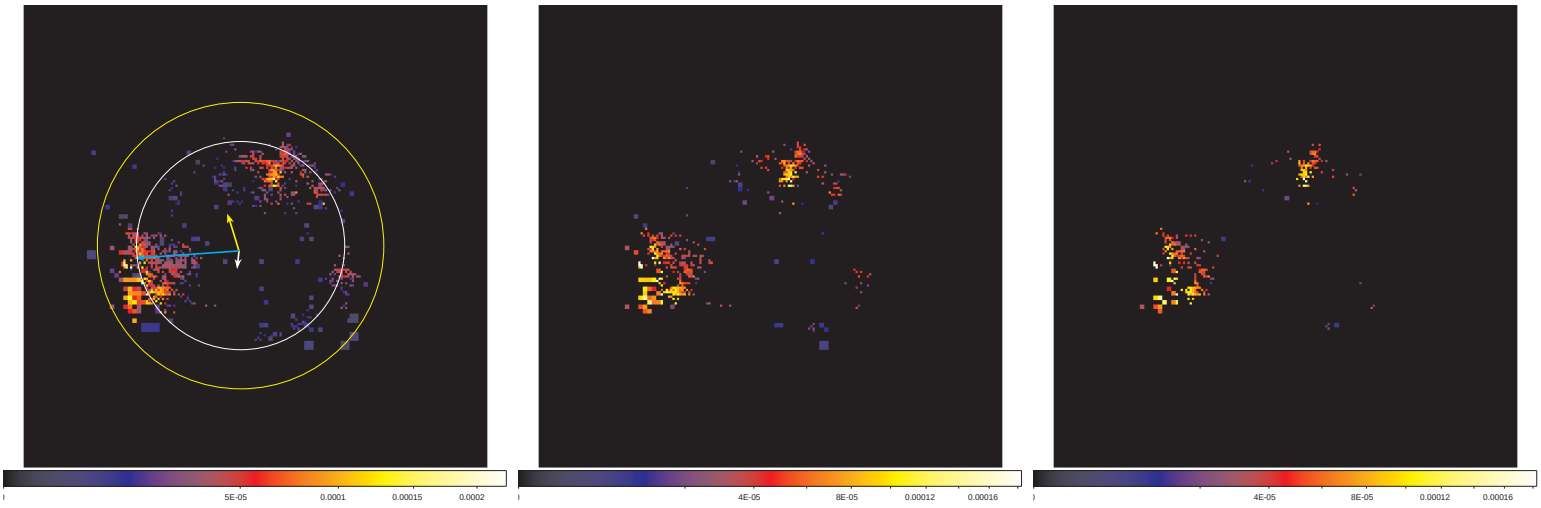

Fig. 6.— The distribution of the added "pure" Fe ejecta component for f-test probability cutoffs of 0.10, 0.01, and 0.001 (left to right). In the left panel, we show fiducial circles showing the radius and position of the forward shock (2.6 pc at 3.4 kpc distance, in yellow) and the contact discontinuity (1.9 pc, in white), and the velocity vectors for the NS (white), the "pure" Fe ejecta (light blue), and total ejecta (yellow) from Table 2 (see subsection 4.2). The circles and velocity vectors are centered at the explosion center of Thorstensen et al. (2001).

Another update corrects the motion of the reverse shock[4]. In previous work we have used a model of the ejecta where a uniform density core is surrounded by a power law envelope. The evolution while the reverse shock is in the outer envelope is given by Chevalier (1982); this solution is then coupled to the known asymptotic behavior of the Sedov-Taylor solution. In this phase, we have previously held the reverse shock speed constant at its value at the envelope-core transition, although it is known that some small acceleration should occur during the core propagation. We now implement a reverse shock acceleration in this phase of evolution following the results given for a suite of models by Patnaude & Fesen (2009). By matching to their results, we write for the reverse shock speed and radius:

$$v_r = \frac{3-s}{n-3}\frac{v_b}{l_{ED}} + \frac{n-6}{43}x_0 t \quad (1)$$

$$R_r = \left[\frac{R_b}{l_{ED}t_{core}} - \frac{3-s}{n-3}\frac{v_b}{l_{ED}}\ln\frac{t}{t_{core}} - \frac{n-6}{43}x_0\left(t - t_{core}\right)\right]t, \quad (2)$$

where $v_r = R_r/t - dR_r/dt$. Here s is the power law index for the CSM density profile, n that for the ejecta envelope, R_b and v_b the forward shock radius and speed, respectively, l_{ED} the "lead factor" (the ratio of forward to reverse shock radii, R_b/R_r), and $x_0 = (40.74M_{ej}/\rho R_b^2)^{1/(3-s)}$, with ρ being the density of the CSM at the forward shock in H atoms (or equivalent mass) per cm^3, t_{core} is the time in years when the reverse shock hits the ejecta core, and M_{ej} is the ejecta mass in solar masses.

In Table 1 we give various models in the range of plausible ejecta masses 2-4 $M_\odot$, all designed to match as far as possible the known dynamics of Cas A. We take a distance of 3.4 kpc (Reed et al. 1995) and an explosion date of 1671.3 ± 0.9 as determined from the proper motions of 17 high velocity outer ejecta knots (Thorstensen et al. 2001). These knots are identified on plates taken as long ago as 1951 and are assumed to be undecelerated, providing the longest time baseline for such studies. More recently, Fesen et al. (2006) have determined a best explosion date of 1681 ± 19 from a sample of 126 relatively undecelerated knots located along the NW limb, observed over a time baseline of 9 months from March to December 2004. With 1671 as the earliest possible explosion date, the remnant age may be up to 333 years in 2004.

Further constraints on the model are provided by the observed shock velocities and radii. A number of authors have made measurements of the expansion rate of Cas A, both for its bright ejecta ring (Vink et al. 1998; Koralesky et al. 1998; DeLaney et al. 2004) and the forward shock (DeLaney & Rudnick 2003). The most recent summary is given by Patnaude

[4]Some other minor modifications and corrections to Appendix A in Laming & Hwang (2003) are collected in the appendix to this paper

& Fesen (2009), who incorporate measurements over the longest time baseline (2000–2007). They find that the expansion is slightly slower in the N and NW filaments, consistent with the known presence of denser CSM on the western limb of Cas A. We take the average expansion 0.31" yr $^{-1}$ from other parts of the remnant, which (at a distance of 3.4 kpc) gives a forward shock velocity of 5050 km s^{-1}. Including all measurements gives a slightly lower average expansion of 0.30" yr^{-1}, and an inferred forward shock velocity of 4850 km s^{-1}.

The forward shock radius is measured from the wispy structures seen in 4-6 keV continuum emission. Gotthelf et al. (2001) use data taken in 2000 and determine an average radius for the northwest sector of 153 ± 12", which translates to 2.52 ± 0.2 pc, but the true shock radius should probably be determined from the outermost of these of these structures rather than the average. Helder & Vink (2008) perform a deconvolution for various azimuthal angle ranges and give a slightly larger forward shock radius of 160" (2.637 pc). There is also a small variation in the radius around the limb. We take a value of 2.6 pc for the forward shock radius in 2004 when the Chandra VLP observation was taken.

The reverse shock radius is harder to quantify. Gotthelf et al. (2001) and Helder & Vink (2008) give a range of radii 1.52 – 1.73 pc, depending on location in the remnant. Morse et al. (2004) measure the reverse shock velocity from proper motions derived from two Hubble Space Telescope WFPC2 images separated by two years. At a reverse shock radius of 106" – 122" (1.75 – 2.01 pc) the reverse shock velocity with respect to the expanding unshocked ejecta is of order ~ 2000 km s^{-1}.

The close match of Cas A's forward shock expansion parameter of 0.66 to the Sedov-Taylor value for expansion into an inverse square density profile has focussed interest in low ejecta mass models that allow faster evolution to the Sedov-Taylor limit. Even so, models generally predict too high a shock velocity and/or too small a radius for the forward shock compared to observations. To increase the forward shock radius, it has been suggested (Hwang & Laming 2009, and see above) that Cas A exploded into a small bubble in the circumstellar medium that developed with a transition from a slow dense red supergiant wind to a fast tenuous wind shortly before explosion. Another possibility is that cosmic ray energy losses at the forward shock provide extra deceleration to suffciently reduce the expansion parameter (Patnaude & Fesen 2009).

The plasma density ahead of the forward shock is derived by Willingale et al. (2003) from fits to XMM data. The baryon mass and filling factor quoted in their Table 3 give a preshock density of hydrogen atoms or equivalent mass of 1.47 cm^{-3}, assuming a shock compression of a factor of 4. Their quoted value for the mass of shocked CSM, 8.31 $M_\odot$, combined with the dimensions outlined above gives a larger preshock density of 1.99 cm^{-3}. These values give the time invariant quantity $\rho r_f^2 = 10 - 13.5$ cm^{-3}pc^2 where the density ρ

at the forward shock is in H atoms (or equivalent mass) cm^{-3} and the forward shock radius r_f is in pc.

Similar results are given by the fits of thermal bremsstrahlung spectra to Suzaku data (Maeda et al. 2009), interpreted as emission from shocked circumstellar medium. The preshock ion number density derived from their thermal bremsstrahlung and power law fit is $2.1/\langle Z^2\rangle$ cm^{-3}, where $\langle Z^2\rangle = \sum_i n_i Z_i^2 / \sum_i n_i Z_i$ is an average charge per ion coming from the thermal bremsstrahlung emissivity. For gas composed of equal number densities of H and He, $\langle Z^2\rangle = 1.7$ and the preshock density is 1.24 cm^{-3} in H atoms of equivalent mass. Taking fit results using thermal bremsstrahlung and SRCut or a cut-off power law gives a higher density of 1.5 cm^{-3} and $\rho r_f^2 = 8.4 - 10$ $\mathrm{cm}^{-3}\mathrm{pc}^2$.

3.2. Cosmic Ray Energy Losses

The expansion parameter for a radiative blast wave can be different from the Sedov-Taylor limit in the case that radiative losses from the shock are significant, or if the shock dissipates energy via cosmic ray acceleration. The two cases may be treated in a similar manner. Following Liang & Keilty (2000) and generalizing to the case of a stellar wind preshock density profile $\rho \propto r^{-s}$, the radius of a radiative blast varies with time as

$$r \propto t^{1/[4-s-(3-s)\alpha]}, \tag{3}$$

where γ is the adiabatic index of the gas, $\alpha = \left\{2 - \gamma + \sqrt{(2-\gamma)^2 + 4(\gamma_1 - 1)}\right\}/4$, and $\gamma_1 = \left\{\sqrt{1 + \epsilon(\gamma^2 - 1)} - 1\right\} \times 2/(\gamma - 1)\epsilon - 1$ is the adiabatic index modified by the loss of a fraction ϵ of the shock energy to radiative (or cosmic ray) losses. If $\epsilon = 0$ so that $\gamma = \gamma_1$, then $\alpha = 1/2$ for all γ and $r \propto t^{2/(5-s)}$. Note that energy going into cosmic rays that remain trapped with their energy in the shock does not change the dynamics, except through modifying γ. If all the shock energy is radiated ($\epsilon = 1$), then $\alpha = 1 - \gamma/2$, and the expansion parameter changes from 0.4 to 0.28 (for $s = 0$) and from 0.67 to 0.55 for $s = 2$, taking $\gamma = 5/3$. Consequently for more modest cosmic ray energy losses, rather small deviations from the unmodified expansion parameter are expected. Cosmic ray energy losses of 10% only change the $s = 2$ expansion parameter from 0.67 to 0.65, decreasing to 0.63 for 30% losses. Patnaude & Fesen (2009) find variations in the expansion parameter of this order.

3.3. The Ejecta Filling Factor

A correction is needed for unresolved density structure in the ejecta. Models of supernova remnants expanding into a stellar wind ($\rho \propto r^{-2}$) density profile generally show a strong density "spike" in the radial direction at the contact discontinuity, and if the reverse shock is still propagating through the outer power law portion of the ejecta density profile, the density at the contact discontinuity is formally infinite (Chevalier 1982). Later in its evolution, the density spike is still present (Chevalier & Oishi 2003), with a width corresponding to about 2 arcsec. This is comparable to or smaller than the size of many of our fit regions, so we expect that ejecta structures will not always be resolved, and a filling factor correction is therefore needed when calculating the plasma electron density (see subsection 4.1 below). We take the volume of each spectral region o be $A^{3/2}$ where A is the area imaged in arcsec^2. This is modified to $A^{3/2}f$, where f is the "filling factor" of the ejecta density profile.

We estimate a quantitative filling factor f to be applied to our fit results in terms of the density scale length L_ρ as $f = L_\rho/\sqrt{A}$.[5] In deriving L_ρ, we follow Hamilton & Sarazin (1984), who give a similarity solution for ejecta structure close to the contact discontinuity. Treating the expansion of uniform density ejecta, they use a coordinate system with $z = 0$ at $r = v_{exp}t$, the outer limit of the ejecta at time t if they were freely expanding without interacting with the reverse shock. The location of the reverse shock is z_s, giving dimensionless Eulerian and Lagrangian coordinates $\zeta = z/z_s$ and $\zeta_0 = z_0/z_s$ respectively, where z_0 is the initial value of z in a Lagrangian plasma element at the time that the plasma was shocked, i.e. z_s at the time of shock passage. With these definitions, close to the contact discontinuity they find (their equation 13)

$$\begin{aligned} \rho &= \rho_s \left(\tfrac{p}{p_s}\right)^{3/5} \zeta_0^{-6/5} \\ \zeta &= V_s \left(\tfrac{p}{p_s}\right)^{-3/5} \tfrac{\zeta_0^\nu}{\nu} + \zeta_c \end{aligned} \tag{4}$$

where $\nu = 23/15$ for a stellar wind external density profile, ζ_c is the value of ζ at the contact discontinuity, and $V_s = 1/12$ is the dimensionless reverse shock velocity. The pressure is p, and p_s is the pressure at the reverse shock. Neglecting the dependence of p on r in this region, we write

$$\frac{\partial\rho}{\partial r} = \frac{\partial\rho}{\partial\zeta_0}\frac{\partial\zeta_0}{\partial\zeta}\frac{\partial\zeta}{\partial r} = \frac{6}{5}\frac{\rho}{z_s V_s}\left(\frac{p}{p_s}\right)^{3/5}\zeta_0^{-\nu} = \frac{6}{5z_s\nu}\frac{\rho}{(\zeta-\zeta_c)} = \frac{\rho}{L_\rho} \tag{5}$$

[5]We are considering emission from a "sheet" of plasma, so only one dimension is compressed, rather than from a clumpy medium, where all three dimensions would require correction.

so that the density scale length $L_\rho = 23\,(\zeta - \zeta_c)\,z_s/18$. We calculate the average of this quantity $\langle L_\rho \rangle = \int_{r_s}^{r_c} \rho L_\rho r^2 dr / \int_{r_s}^{r_c} \rho r^2 dr$ using

$$\begin{aligned}
\int_{r_s}^{r_c} \rho r^2 dr &= \int_{r_s}^{r_c} \left(\frac{p}{p_s}\right)^{3/5} \rho_s \zeta_0^{-6/5} r^2 dr = \rho_s \left(\frac{p}{p_s}\right)^{(3/5-12/23)} \left(\tfrac{5 z_s}{92}\right)^{18/23} \int_{r_s}^{r_c} r^2\,(r_c - r)^{-18/23} dr \\
\int_{r_s}^{r_c} L_\rho \rho r^2 dr &= \tfrac{23 z_s}{18} \int_{r_s}^{r_c} \left(\frac{p}{p_s}\right)^{3/5} \rho_s \frac{(\zeta - \zeta_c)}{\zeta_0^{6/5}} r^2 dr = \rho_s \left(\frac{p}{p_s}\right)^{(3/5-12/23)} \left(\tfrac{5 z_s}{92}\right)^{18/23} \tfrac{23}{18} \int_{r_s}^{r_c} r^2\,(r_c - r)^{5/23} dr \quad (6)
\end{aligned}$$

The integrals are evaluated using the substitution $u = r_c - r$, with the final result

$$\langle L_\rho \rangle = \frac{23}{18} \left\{ \frac{\frac{23}{18}\,(1 - r_s/r_c)^{28/23} - \frac{46}{51}\,(1 - r_s/r_c)^{51/23} + \frac{23}{74}\,(1 - r_s/r_c)^{74/23}}{\frac{23}{5}\,(1 - r_s/r_c)^{5/23} - \frac{23}{14}\,(1 - r_s/r_c)^{28/23} + \frac{23}{51}\,(1 - r_s/r_c)^{51/23}} \right\} r_c. \quad (7)$$

Including the variation of p, L_ρ in equation 5 is modified to

$$L_\rho = z_s\,(\zeta - \zeta_c) \left\{ \frac{5\nu/3 - \partial \ln p / \partial \ln \zeta_0}{2 - \partial \ln p / \partial \ln \zeta_0} \right\}. \quad (8)$$

From Table 1 of Hamilton & Sarazin (1984), $\partial \ln p / \partial \ln \zeta_0$ varies from -1 at the reverse shock to about -0.6 at the contact discontinuity, which reduces the value for L_ρ derived assuming $\partial \ln p / \partial \ln \zeta_0 = 0$ by 5% to 7%. For completeness, if the external density $\propto r^{-3}$, then $\nu = 6/5$ and $L_\rho = z_s\,(\zeta - \zeta_c) = r_c - r$, independent of $\partial \ln p / \partial \ln \zeta_0$. The filling factor is then calculated as $f = L_\rho / \sqrt{A}$, with L_ρ and A here expressed in arcsec and arcsec^2 respectively.

As we will show below, our data suggest that many secondary shocks reflect from the blast wave and reverse shock as they encounter density inhomogeneities in Cas A. We therefore use equation 7 with the tacit assumption of constant pressure near the contact discontinuity. Truelove & McKee (1999) point out that this approximation is also made by Hamilton & Sarazin (1984) in their energy equation. With $r_s/r_c = 0.9$ we find $L_\rho = 0.021 r_c = 1.26 \times 10^{17}$ cm, which at a distance of 3.4 kpc subtends an angle of 2.48 arcsec. In this last step we are extrapolating slightly out of the formal range of validity of the Hamilton & Sarazin (1984) model. There, $z_c/z_s = (v_{exp} t - r_c)\,/\,(v_{exp} - r_s t) = 0.953$, which requires an expansion velocity of the outermost ejecta greater than 20,000 km s^{-1} for values of $r_c = 1.95$ pc and $r_s = 1.7$ pc appropriate for Cas A. It is also worth bearing in mind other caveats to the application of this model. Hamilton & Sarazin (1984) assume uniform density ejecta, while we adopt the prescription of Truelove & McKee (1999) of a core-envelope density profile. We have also introduced the circumstellar "bubble" into which Cas A is assumed to have exploded.

4. Discussion

4.1. The Elemental Composition of the Cas A Ejecta

In previous works (Laming & Hwang 2003; Hwang & Laming 2003) we have discussed the use of models of SNR evolution to interpret the fitted ionization age of ejecta spectra in terms of the time elapsed since reverse shock passage, hence allowing the inference of a Lagrangian mass coordinate. This is successful in a limited number of carefully selected regions of Cas A, but is evidently not the case in general. Figure 2 shows the ionization age value strongly peaked near $\log(n_e t) \simeq 11.3$, which implies that all the ejecta are piled up at a mass coordinate of 0.2 (where 0 marks the center of the ejecta and 1.0 the outermost extent), instead of being uniformly distributed with mass coordinate. We suggest that this must arise from the interaction of the reverse shocked ejecta with secondary shocks propagating within the SNR shell. These arise as the forward and reverse shocks encounter density inhomogeneities, sending a transmitted shock through the density structure together with a reflected shock back into the previously shocked gas. Such a scenario has previously been considered (Laming 2001a,b) as a possibility for electron acceleration with a view to explaining the hard X-ray emission of Cas A. More recently, Inoue et al. (2010) consider a similar model for ion acceleration at shocks.

Taking a typical electron density of 200 cm^{-3} (Lazendic et al. 2006, and see below), an ionization age of 2×10^{11} cm^{-3}s implies a shock interaction around 30 years prior to the observation. Given this "obscuration" of the ionization age determined by the reverse shock, we estimate the density in each fit region from the emission measure assuming

$$EM = \sum_i n_i n_e Z_i^2 V = n_e V \sum_i n_i Z_i^2 = n_e^2 V \left\langle Z^2 \right\rangle \tag{9}$$

where $\langle Z^2 \rangle = \sum_i n_i Z_i^2 / \sum_i n_i Z_i = \sum_i n_i Z_i^2 / n_e$, and the sum i is over all ions in the plasma. The plasma volume is V. The plasma electron density then follows with an appropriate assumption about V. The simplest assumption that $V = A^{3/2}$ (where A is the area on the sky of the fit region chosen), and we modify this to $V = A^{3/2} \times f$ where f is the filling factor discussed previously.

The ejecta mass in each imaged region is estimated as $EM/n_e/\langle Z^2 \rangle \times \sum_i n_i m_i / n_e$, from which the masses of individual elements are obtained as fractions of the total ejecta mass from the fitted element abundances. In Table 2 we give the masses of O, Ne, Mg, Si, S, Ar, and Fe resulting from our fits, for assumed filling factors corresponding to a density spike thickness of 2.5" and 5"; the latter arises as one observes the SNR ejecta shell in both front and back along the same line of sight. In this latter case, the complete X-ray emitting ejecta mass inferred is 2.84 $M_\odot$, and the total ejecta mass including unshocked ejecta is 3.14 $M_\odot$

with reference to Table 1; this gives a value of ρr_f^2 from Table 1 at the upper end of values inferred elsewhere as discussed in section 3.1. Extrapolation to other cases is simple, since element masses are proportional to $\sqrt{f}$. Table 2 also gives plane of the sky velocities for each element (calculated from the position of the center of mass of each element, and assuming homologous expansion), and for the SNR as a whole, and compares abundance ratios relative to O with solar system values.

We also comment here that Cas A is thought to have retained some H at the time of explosion (Fesen 2001; Fesen & Becker 1991; Chevalier & Oishi 2003), and this may contribute to the thermal bremsstrahlung emission here attributed to O. In this case, our ejecta mass estimate would be an underestimate, and if the H were not uniformly distributed, the recoil velocity we attribute to the O ejecta could be in error. It is difficult to assess an uncertainty here, but we note that the amount of H involved is likely rather small and unlikely to alter our conclusion of an approximately 3 $M_\odot$ ejecta mass.

In Table 3 we give the masses of Fe associated with incomplete Si-burning, and the "pure" component, the latter arising either from complete Si-burning or α-rich freeze out, for a variety of assumptions about the statistical significance of requiring the second fit component. We calculate the F-distribution following Press et al. (1992) and evaluate the probability that the second component is not justified by the improvement in χ^2, i.e. the probability that the residuals from the fit with and without the second component are statistically from the same distribution. Note that in Table 2 we have taken those Fe masses corresponding to a probability of 0.01.

4.2. The Mass and Distribution of Fe

Our analysis of more than 4300 ejecta regions gives a mass of Fe in the Cas A ejecta of $\sim 0.08 - 0.14 M_\odot$, depending on the assumed filling factor and threshold probability for acceptance of the "pure" Fe component. This mass is comparable to that expected (Eriksen et al. 2009), but gives only the Fe detected in the reverse shocked X-ray emitting ejecta. According to our models, an extra 0.18 - 0.3 $M_\odot$ of ejecta may be unshocked, interior to the reverse shock, and visible primarily in the infra-red.

Infrared observations with Spitzer do show emission at the center of the remnant that is believed to be from unshocked ejecta, but of [Si II]. As discussed by DeLaney et al (2010), it is coincident with free-free absorption seen in the radio by Kassim et al. (1995), and appears to correspond to cool (< 1000 K), low density gas that has been photoionized. DeLaney et al. conclude, however, that it is unlikely that a significant fraction of these unshocked ejecta

could be Fe. Relatively little infra-red Fe emission is observed at all in the remnant, and the main [Fe II] line at 26 μ is blended with [O IV]. Isensee et al. (2010) demonstrate that [O IV] is more plausibly the dominant component of this blend, though they do claim a 2σ detection of [Fe II] from the center when all spatial bins are summed. Unblended [Fe II] emission at 17.94 μm (Ennis et al. 2006) and 1.64 μm (Rho et al. 2003) is also detected, but appears to be associated primarily with the bright ejecta ring, and not the interior. [Fe II] lines are also absent or very weak in optical and near infra-red observations of Cas A ejecta knots. Hurford & Fesen (1996) only report marginal detections of [Fe II] 8617 Å in spectra of fast moving knots (FMKs), and Gerardy & Fesen (2001) report similarly on the [Fe II] lines between 1 and 2 μm in FMKs, although these transitions are easily detected in the spectra of quasi-stationary flocculi (QSFs). Eriksen et al. (2009) do detect [Fe II] 1.257 μm and 1.644 μm lines from 15 FMKs and 4 QSFs, from which they estimate the reddening.

Further consideration of the dust in Cas A sheds light on the possible presence of unshocked Fe. Large masses of cold dust had been reported in Cas A from submillimeter observations (Dunne et al. 2003), but it has been pointed out that some of the detected emission originates from foreground molecular clouds (Krause et al. 2004; Wilson & Batrla 2005). This emission can also be explained with $< 10^{-3}$ $M_\odot$ of conducting dust needles (i.e., Fe) that are formed in the ejecta (Dwek 2004). Rho et al. (2008) favor FeO dust to explain the Spitzer infrared spectra and conclude that Fe dust may be present at masses up to $10^{-2} M_\odot$. More recently, Nozawa et al. (2010) suggest the presence of significant quantities of cool dust, a conclusion that is supported by recent infrared observations with Herschel (Barlow et al. 2010), AKARI and BLAST (Sibthorpe et al. 2010). The cool dust has a temperature of about 35 K based on the infrared flux densities, and is presumably unshocked ejecta as it is confined to the central regions of the remnant. The emission is consistent with a silicate dust composition, and the inferred dust mass is about 0.06-0.075 $M_\odot$. Nozawa et al. (2010)'s calculations are for dust formation in a Type IIb event (with an eye toward Cas A) and indicate that little dust would be associated with the innermost Fe-Ni layer due to the extended radioactive heating: the gas density drops too low before the temperatures are low enough for Fe or Ni grains to condense. Up to about $10^{-3} M_\odot$ of Fe could be locked up in FeS grains, but highly Fe-rich ejecta would not necessarily have a dust signature, as appears to be borne out by the infrared observations. Cherchneff & Dwek (2010) take a chemical kinetic approach and find rather more FeS grain formation in a 20 $M_\odot$ model SN with unmixed ejecta (the most appropriate of the cases they consider for Cas A), with about 0.021 $M_\odot$ of Fe in FeS. A mass this high is unlikely for Cas A, however, given that its highly stripped progenitor underwent a Type IIb event. Dust will form relatively more efficiently in a normal Type II event because the overlying stellar envelope restricts ejecta expansion and preserves higher densities favorable for dust condensation.

We are left with the surprising conclusion that almost all of the Fe ejected by the supernova is now well outside the reverse shock and visible in X-rays, with very little left in the center of the remnant. This is true even for the "pure" Fe component, which we take to be the ashes of α-rich freezeout. An initial mass of ^{44}Ti of $1.6 \times 10^{-4} M_{\odot}$ has been inferred for Cas A from observations with the Compton Gamma Ray Observatory/COMPTEL (Iyudin et al. 1994), BeppoSAX and the INTEGRAL IBIS/ISGRI instrument (Vink et al. 2001; Renaud et al. 2006). Based on spherically symmetric simulations, designed to match the Cas A progenitor (Young et al. 2006; Eriksen et al. 2009), Magkotsios et al. (2010) predict $\sim 10^{-4} M_{\odot}$ of ^{44}Ti, and 0.25 $M_{\odot}$ of ^{56}Ni. These are both within a factor of 1.6 of measured values (taking the 5" filling factor in Table 2), but are discrepant in opposite directions so that the mass ratio ^{56}Ni/^{44}Ti$\simeq$ 2500 compared with the observed ratio of $\sim 10^3$. A similar outcome of the earlier calculations of The et al. (1998) and others (reviewed in The et al. 2006) led Nagataki et al. (1998) to suggest that this ratio may be reduced in an asymmetrical explosion. Magkotsios et al. (2010) also enable an estimate of the Fe formed in α-rich freeze out compared with that formed in incomplete Si-burning. Their Figure 17 suggests that approximately half the Fe should be associated with a mass ratio ^{56}Fe/^{28}Si$>$ 10 and half with ^{56}Fe/^{28}Si$<$ 10. In our Table 3, taking probabilities between 0.1 and 0.01, we would infer that approximately 1/3 of the Fe should have formed in α-rich freeze out and thus be in regions with very small ^{28}Si masses.

In Cas A, the ionization age of $> 10^{11.3}$ cm^{-3}s places the "pure" Fe at least 0.75 $M_{\odot}$ out from the center in 3 $M_{\odot}$ of ejecta. According to Magkotsios et al. (2010), this would place it well outside the ejecta region where it was formed, into the outer layers where the composition would originally have been dominated by O, Si, C, and Ne. The fact that essentially all of the Fe is found at such locations, and not in the center of the remnant inside the reverse shock suggests the operation of a strong instability.

The ^{44}Ti should also be expected to be well outside the reverse shock, spatially coincident with the pure Fe, which should be confirmed by observations with NUSTAR (Harrison et al. 2010). This is quite different to the case of SN 1987A, where the ejecta are currently heated by the decay chain of ^{44}Ti, which appears to be located in the center of the remnant, with ballistic expansion velocity of order 3000 km s^{-1} (Kjaer et al. 2010). G1.9+0.3 (Borkowski et al. 2010) is more like Cas A in this respect, with most of its ^{44}Ti in an X-ray bright region beyond the reverse shock, and a smaller mass of ^{44}Ti in the unshocked interior. Considering the young age and fast expansion of G1.9+0.3, this may mean that ^{44}Ti has been mixed out even further into the ejecta than is the case in Cas A, although the SN origin of G1.9+0.3 is unknown.

We are unable to derive reliable line-of-sight velocities from the Chandra data, but some

insight into the motion of the "pure" Fe component can be gained from the motion of ^{44}Ti observed with INTEGRAL (Martin & Vink 2008; Martin et al. 2009). The SPI instrument measures the width and the shift of the 1157 keV decay line of ^{44}Ca, which is the final step in the chain of decays from ^{44}Ti. It is found that the ^{44}Ti is receding from the observer with a velocity of about 500 km s^{-1}, and has an intrinsic width, or velocity dispersion, of 430 km s^{-1}. Since the expansion velocity of the Fe is close to 4000 km s^{-1}, if the Fe associated with the ^{44}Ti, it must be expanding in a direction close to the plane of the sky. The velocity dispersion indicates that the ^{44}Ti presumably occupies a volume significantly smaller than that outlined by the "pure" Fe, with a half angle subtended at the explosion center of order $\sin^{-1}(430/4000) \simeq 6$ degrees.

4.3. The Neutron Star Kick

The neutron star is known to be recoiling from the explosion center inferred from the optical knot motions with a velocity in the plane of the sky of 330 km s^{-1} (Thorstensen et al. 2001). The direction of recoil is also nearly perpendicular from the NE-SW axis established by the jet and counter-jet, which presumably delineate an axis of rotation in the progenitor. This makes a kick arising from the action of a standing accretion shock instability appealing. It is known, at least in the limit of slow rotation, where distortion of the shock front from spherical symmetry can be neglected, that the instability grows fastest in the prograde spiral mode (e.g. Blondin & Mezzacappa 2007; Yamazaki & Foglizzo 2008; Iwakami et al. 2009), i.e., perpendicular to the symmetry axis. The pulsar kick imparted by the second supernova that formed the double pulsar system PSR B1913+16 is also inferred to have been largely perpendicular to the progenitor spin axis (Wex et al. 2000). The magnitude of the observed recoil velocity is also well within the accessible range generated by numerical simulations of such instabilities, albeit these are so far for initially nonrotating supernova cores (Wongwathanarat et al. 2010; Nordhaus et al. 2010). At higher rotation rates, it appears that the instability is suppressed (Burrows et al. 2007), though the deformation of the accretion shock by rotation may seed an axisymmetric quadrupole oscillation (Iwakami et al. 2009).

In the case that the kick involves instability at the accretion shock, following the suspicion advanced by Wongwathanarat et al. (2010), we would expect the Fe ejecta to recoil predominantly in the opposite direction to the neutron star. In Cas A, this appears not to be the case. Most of the Fe, and especially most of the "pure" Fe, is recoiling towards the east, within 90 degrees of the neutron star motion. However, the remnant as a whole, whose mass is dominated by O, is actually recoiling to the north, close to 150 degrees from the neutron

star motion, with a plane of the sky velocity of about 700 km s^{-1}, which perhaps suggests a hydrodynamic origin for the kick. Wongwathanarat et al. (2010) discuss a 15 $M_{\odot}$ explosion, whereas the Cas A progenitor was considerably less massive upon explosion such that reverse shocks and associated nucleosynthesis during the explosion are less likely to occur. Our estimate of the remnant recoil assumes homologous expansion, and the approximations made in assessing the ejecta mass have been detailed in sections 3 and 4.1.

5. Conclusions

We consider our efforts here to be a *first* attempt at a comprehensive view of the X-ray emitting ejecta in Cas A on few arcsecond angular scales. We have carried out at considerable effort the most detailed data analysis that was practicable for us, but there is ample room for improvement. The most obvious shortcoming of this work is the need for a more sophisticated definition of spectral extraction regions, and hand-in-hand with that, yet more extraction regions. In previous work, we had individually chosen regions to correspond to identifiable knotty or filamentary features. Here we were obliged for the sake of (relative) expediency to instead use regions that, while adjusted crudely for overall surface brightness, have been defined without reference to coherent structures in the surface brightness. Full use of the Chandra angular resolution in fact requires a more sophisticated definition of the extraction regions. The main advantage to be obtained, however, is that this may allow the use of simpler NEI models with a single ionization age, rather than parallel shock models with a linear distribution of ionization ages, and thus a much clearer connection with analytical hydrodynamical models (see for example, Laming & Hwang 2003; Hwang & Laming 2003). It may also eliminate the requirement for the filling factor correction used here. Finally, the analysis would also benefit from a more sophisticated treatment of the spectral background.

We have arrived at a favored ejecta mass of about 3 $M_{\odot}$ based both on the observed SNR dynamics, and on an accounting of the X-ray emission and element abundances throughout the remnant. The increased signal/noise afforded by the long exposure time, and by the relatively large size of extraction regions has allowed us to identify regions of the remnant where the Fe ejecta is to a large extent "pure", in that the mass ratio Fe/Si > 10. We seek to interpret this ejecta component as alpha-rich freeze out ashes, where the recently discovered (Iyudin et al. 1994; Vink et al. 2001; Renaud et al. 2006) ^{44}Ti and its decay products likely reside. The surprise here is that essentially all the Fe, and presumably also the ^{44}Ti and its decay products, are not located in the center of the remnant but have been ejected well out into the overlying ejecta, probably by the action of hydrodynamic instabilities during the explosion. In this respect, SN 1987A offers a stark contrast, with ejecta containing ^{44}Ti

located at the center with a characteristic expansion speed of ~ 3000 km s^{-1} (Kjaer et al. 2010). G1.9+0.3 may represent an intermediate case (Borkowski et al. 2010).

Finally, Cas A has a well documented displacement of the neutron star formed in the explosion (Thorstensen et al. 2001), which is close to perpendicular to the NE-SW "jet"-axis. While contrary to expectations (e.g. Wongwathanarat et al. 2010), the Fe in Cas A does not recoil in the opposite direction to the neutron star, as far as we can tell, but the remnant as a whole does. We take this as reinforcing the notion that neutron star kicks in core-collapse supernova explosions may derive from purely hydrodynamic mechanisms, as recently suggested (e.g. Nordhaus et al. 2010). Together with motion and location of the Fe ejecta, and the likelihood that what is observed as a NE-SW "jet" really is an artefact of an asymmetric explosion, we speculate that an instability of the standing accretion shock (SASI) in a rotating progenitor is the most promising model for understanding the explosion that formed Cas A.

We gratefully acknowledge support through NASA grants to the Chandra Guest Observer Program and NNH04ZSS001N to the Long Term Space Astrophysics Program. JML was also supported by basic research funds of the Office of Naval Research.

A. Revisions to Appendix A in Laming & Hwang (2003)

We collect here a few minor corrections and modifications to the text in Appendix A of Laming & Hwang (2003). Equations A1 and A2 should read

$$t_0 = 473.6 M_{ej}^{5/6} E_{51}^{-1/2} \rho^{-1/3} \mathrm{yr}, \tag{A1}$$

$$x_0 = 3.43 M_{ej}^{1/3} \rho^{-1/3} \mathrm{pc}. \tag{A2}$$

The expressions for the lead factor and the pressure ratio between forward and reverse shocks following equation A5 are now more accurately given by

$$l_{\mathrm{ED}} = 1.0 + \frac{8}{n^2} + \frac{0.4}{4-s} \tag{A3}$$

$$\phi_{\mathrm{ED}} = (0.65 - \exp(-n/4)) \sqrt{1 - s/8}. \tag{A4}$$

Finally, as pointed out to us by Elisabetta Micelotta, some of the discussion following equation A8 in Laming & Hwang (2003) requires clarification. Equation A5 can be derived from the envelope form of equation A8, i.e. from equations A7 and A8 in Truelove & McKee

(1999). This procedure requires $v_{ej} = \sqrt{(10/3)\,(n-5)\,/\,(n-3)}$ going from equation 74 to 75 in Truelove & McKee (1999). In their equation 31, Truelove & McKee (1999) give $v_{core} = \sqrt{(10/3)\,(n-5)\,/\,(n-3)}$, which implies $w_{core} = v_{core}/v_{ej} = 1$. However their derivation of equation 31 assumes $w_{core} \to 0$ in their derivation. A "cleaner" route to equation 75 of Truelove & McKee (1999) is to take their values of v_{core} and the ejecta mass fraction in the core derived under the condition $w_{core} \to 0$, and substitute into equation 3 of Chevalier (1982). The condition $R_b = l_{\rm ED} v_{core} t_{core}$ still gives the time t_{core} when the reverse shock hits the ejecta core. The only other change connected with this discussion is that equation A11 for t_{conn} in Laming & Hwang (2003) should depend on v_{core} and not v_{ej}.

In actual fact, the difference between the approximations $w_{core} = 0$ and $w_{core} = 1$ is not all that large; $v_{core} = \sqrt{(10/3)\,(n-5)\,/\,(n-3)} \to \sqrt{2}$ in these limits, which coincide for $n = 8$. The core fraction of the ejecta mass varies between $(n-3)\,/n$ and 1, and only v_{ej} which goes from ∞ to v_{core} between these two limits is sensitive.

REFERENCES

Anders, E., & Grevesse, N. 1989, Geochim. Cosmochim. Acta, 53, 197

Arnett, D., & Meakin, C. 2011, arXiv:1101.5646

Arnett, D. 1996, Supernovae and Nucleosynthesis, (Princeton University Press: Princeton, NJ)

Arzoumanian, Z., Chernoff, D. F., & Cordes, J. M. 2002, ApJ, 568, 289

Barlow, M. J., et al. 2010, A&A, 518, L138

Borkowksi, K. J., Reynolds, S. P., Green, D. A., Hwang, U., Petre, R., Krishnamurthy, K., & Willett, R. 2010, ApJ, 724, L161

Borkowski, K. J., Lyerly, W. J., & Reynolds, S. P. 2001, ApJ, 548, 820

Blondin, J. M., & Mezzacappa, A. 2007, Nature, 445, 58

Blondin, J. M., Mezzacappa, A., & DeMarino, C. 2003, ApJ, 584, 971

Brandt, T. D., Burrows, A., Ott, C. D., & Livne, E. 2011, ApJ, 728, 8

Burrows, A., Dessart, L., Livne, E., Ott, C. D., & Murphy, J. 2007, ApJ, 664, 416 J. 1996, Phys. Rev. Lett., 76, 352 Hayes, J., & Fryxell, B. A. 1995, ApJ, 450, 830

Cherchneff, I., & Dwek, E. 2010, ApJ, 713, 1

Chevalier, R. A. 1982, ApJ, 258, 790

Chevalier, R. A., & Kirshner R. P. 1978, ApJ, 219, 931

Chevalier, R. A., & Oishi, J. 2003, ApJ, 593, L23

DeLaney, T. A. & Rudnick, L. 2003, ApJ, 589, 818

DeLaney, T., et al. 2010, ApJ, 725, 2038

DeLaney, T., Rudnick, L., Fesen, R. A., Jones, T. W., Petre, R., & Morse, J. A. 2004, ApJ, 613, 343

Dunne, L., Eales, S., Ivison. R., Morgan, H., & Edmunds, M. 2003, Nature, 424, 285

Dwek, E., & Arendt, R. G. 2008, ApJ, 685, 976

Dwek, E. 2004, ApJ, 607, 848

Ennis, J., et al. 2006, ApJ, 652, 376

Eriksen, K. A., Arnett, D., McCarthy, D. W., & Young, P. 2009, ApJ, 697, 29

Faucher-Giguère, C.-A., & Kaspi, V. M. 2006, ApJ, 643, 332

Fesen, R. A., et al. 2006, ApJ, 645, 283

Fesen, R. A. 2001 ApJS, 133, 161

Fesen, R. A., & Becker, R . H. 1991, ApJ, 371, 621

Foglizzo, T., Galletti, P., Scheck, L., & Janka, H.-T. 2007, ApJ, 654, 1006

Gerardy, C. L., & Fesen, R. A. 2001, AJ, 121, 2781

Gotthelf, E. V., Koralesky, B., Rudnick, L., Jones, T. W., Hwang, U., & Petre, R. 2001, ApJ, 552, L39

Hamilton, A. J. S., & Sarazin, C. L. 1984, ApJ, 281, 682

Hammell, M. C., & Fesen, R. A. 2008, ApJS, 179, 195

Harrison, F. A., et al., 2010, Proc. SPIE 7732, 77320S-1

Helder, E., & Vink, J. 2008, ApJ, 686, 1094

Herant, M., Benz, W., & Colgate, S. 1992, ApJ, 395, 642

Herant, M. 1995, Phys. Rep., 256, 117

Hines, D. C., et al. 2004, ApJS, 154, 290

Hobbs, G., Lormier, D. R., Lyne, A. G., & Kramer, M. 2005,MNRAS, 360, 974

Hughes, J. P., Rakowski, C. E., Burrows, D. N., & Slane, P. O. 2000, ApJ, 528, L109

Hurford, A. P., & Fesen, R. A. 1996, ApJ, 469, 246

Hwang, U., Holt, S. S., & Petre, R. 2000 ApJ, 537, L119

Hwang, U., & Laming, J. M. 2003, ApJ, 597, 362

Hwang, U., et al. 2004, ApJ, 615, L117

Hwang, U., & Laming, J. M. 2009, ApJ, 703, 883

Inoue, T., Yamazaki, R., & Inutsuka, S.-I. 2010, ApJ, 723, L108

Isensee, K., Rudnick, L., DeLaney, T., Smith, J. D., Rho, J., Reach, W. T., Kozasa, T., & Gomez, H. 2010, ApJ, 725, 2059

Iwakami, I., Kotake, K., Ohnishi, N., Yamada, S., & Sawada, K. 2009, ApJ, 700, 232

Iyudin, A. F., et al. 1994, A&A, 284, L1

Kassim, N. E., Perley, R. A., Dwarakanath, K. S., & Erickson, W. C. 1995, ApJ, 455, L59

Keohane, J. W., Rudnick, L., & Anderson, M. C. 1996, ApJ, 466, 309

Kjaer, K., Leibundgut, B., Fransson, C., Jerkstrand, A., & Spyromilio, J. 2010, A&A, 517, A51

Koralesky, B., Rudnick, L., Gotthelf, E. V., & Keohane, J. W. 1998, ApJ, 505, L27

Krause, O., et al. 2004, Nature, 432, 596

Laming, J. M. 2001a, ApJ, 546, 1149

Laming, J. M. 2001b, ApJ, 563, 828

Laming, J. M., Hwang, U., Radics, B., Lekli, G., & Takács, E. 2006, ApJ, 644, 260

Laming, J. M., & Hwang, U. 2003, ApJ, 597, 347

Lazendic, J. S., Dewey, D., Schulz, N. S., & Canizares, C. R. 2006, ApJ, 651, 250

Leonard, D. C., et al. 2006, Nature, 440, 505

Liang, E., & Keilty, K. 2000, ApJ, 533, 890

Maeda, Y., et al. 2009, PASJ, 61, 1217

Magkotsios, G., Times, F. X., Hungerford, A. L., Fryer, C. L., Young, P. A., & Wiescher, M. 2010, ApJS, 191, 66

Markert, T. H., Clark, G. W., Winkler, P. F., & Canizares, C. R. 1983,ApJ, 268, 134

Martin, P., & Vink, J. 2008, New Astronomy Reviews, 52, 401

Martin, P., Knödlseder, J., Vink, J., Decourchelle, A., & Renuad, M. 2009, A&A, 502, 131

Mauche, C. W., & Gorenstein, P. 1989, ApJ, 336, 843

Mazzali, P. A., Deng, J., Nomoto, K., Sauer, D. N., Pian, E., Tominaga, N., Tanaka, M., Maeda, K., & Filippenki, A. V. 2006, Nature, 442, 1018

Morrison, R., & McCammon, D. 1983, ApJ, 270, 119

Morse, J. A., Fesen, R. A., Chevalier, R. A., Borkowski, K. J., Gerardy, C. L., Lawrence, S. S., & van den Bergh, S. 2004, ApJ, 614, 727

Nagataki, S., Hashimoto, M., Sato, K., Yamada, S., & Mochizuki, Y. S. 1998, ApJ, 492, L45

Nordhaus, J., Brandt, T. D., Burrows, A., Livne, E., & Ott, C. D. 2010, Phys. Rev. D, 82, 103016

Nozawa, T., Kozasa, T., Tominaga, N., Maeda, K., Umeda, H., Nomoto, K., & Krause, O. 2010, ApJ, 713, 356

Ott, C. D., Burrows, A., Dessart, L., & Livne, E. 2008, ApJ, 685, 1069

Patnaude, D., J., & Fesen, R. A. 2009, ApJ, 697, 535

Predehl, P., & Schmitt, J. H. M. M. 1995, A&A, 293, 889

Press, W. H., Teukolsky, S. A., Vetterling, W. T., & Flannery, B. P. 1992, Numerical Recipes, (Cambridge University Press: Cambridge UK)

Reed, J. E., Hester, J. J., Fabian, A. C., & Winkler, P. F. 1995, ApJ, 440, 706

Renaud, M., et al. 2006, ApJ, 647, L41

Rest, A., et al. 2011, ApJ, 732, 3

Rho, J., Kozasa, T., Reach, W. T., Smith, J. D., Rudnick, L., DeLaney, T., Ennis, J. A., Gomez, H., & Tappe, A. 2008, ApJ, 673, 271

Rho, J.-H., et al. 2003, ApJ, 592, 299

Scheck, L., Plewa, T., Janka, H. -T., Kifonidis, J., & Müller, E. 2004, PRL, 92, 011103

Sibthorpe, B., et al. 2010, ApJ, 719, 1553

Stage, M. D., Allen, G. E., Houck, J. C., & Davis, J. E. 2006, Nature Physics, 2, 614

The, L.-S., Clayton, D. D., Jin, L., & Meyer, B. S. 1998, ApJ, 504, 500

The, L.-S., Clayton, D. D¿, Diehl, R., Hartmann, D. H., Iyudin, A. F. ,Leising, M. D., Meyer, B. S., Motizuki, Y., & Schönfelder, V. 2006, A&A, 450, 1037

Thorstensen, J. R., Fesen, R. A., & van den Bergh, S. 2001, AJ, 122, 297

Truelove, J. K., & McKee, C. F. 1999, ApJS, 120, 299

Vink, J. 2004, New Astronomy Review, 48, 61

Vink, J., Laming, J. M., Kaastra, J. S., Bleeker, J. A. M., Bloemen, H., & Oberlack, U. 2001, ApJ, 560, L79

Vink, J., Bloemen, H., Kaastra, J. S., & Bleeker, J. A. M. 1998, A&A, 339, 201

Vink, J., Kaastra, J. S., & Bleeker, J. A. M. 1996, A&A, 307, L41

Wex, N., Kalogera, V., & Kramer, M. 2000, ApJ, 528, 401

Willingale, R., Bleeker, J. A. M., van der Heyden, K. J & Kaastra, J. S. 2002, A&A, 381, 1039

Willingale, R., Bleeker, J. A. M., van der Heyden, K. J., & Kaastra, J. S. 2003, A&A, 398, 1021

Wilson, T. L., & Batrla, W. 2005, A&A, 430, 561

Wongwathanarat, A., Janka, H.-T., & Müller, E. 2010, ApJ, 725, L106

Yamazaki, T., & Foglizzo, T. 2008, ApJ, 679, 607

Young, P. A., Fryer, C. L., Hungerford, A., Arnett, D., Rockefeller, G., Timmes, F. X., Voit, B., Meakin, C., & Ericksen, K. A. 2006, ApJ, 640, 891

Table 1: Model Parameters

$M_{ej}/M_\odot$	E_{51}	v_b	R_b	v_r	R_r	ρr_f^2	R_{bub}	v_{exp}	$M_{ej,x}/M_\odot$	m	age	v_{core}
2.0	1.7	5376	2.6	2611	1.65	10	0.26	4900	1.84	0.694	328.7	10086
2.5	2.0	5330	2.6	2509	1.67	12	0.28	4924	2.28	0.697	332.6	9785
3.0	2.35	5357	2.6	2465	1.70	14	0.30	5012	2.71	0.699	331.6	9683
3.5	2.67	5353	2.6	2416	1.73	16	0.33	5099	3.13	0.699	331.9	9555
4.0	3.0	5357	2.6	2384	1.75	18	0.35	5163	3.55	0.699	331.8	9474

Note. — Table columns give in order: M_{ej} ejecta mass ($M_\odot$), E_{51} explosion energy (10^{51} ergs), v_b forward shock velocity (km s^{-1}), R_b forward shock radius (pc), v_r reverse shock velocity (km s^{-1}), R_r reverse shock radius (pc), ρr_f^2 density times forward shock radius at the current position of the forward shock in H atoms (or equivalent mass)$\times$ pc^2, R_{bub} circumstellar bubble radius (pc), v_{exp} ejecta expansion velocity at reverse shock (km s^{-1}), $M_{ej,x}$ mass of X-ray emitting ejecta ($M_\odot$), m expansion parameter, SNR age (years), and v_{core} expansion velocity of ejecta core-envelope boundary (km s^{-1}).

Table 2: Element Masses, Velocities

element	$M_{el,2.5''}/M_\odot$	$M_{el,5''}/M_\odot$	v_x	v_y	M_{el}/M_O	$M_{el}/M_O\|_{solar}$
O	1.80	2.55	-176	706	1.00	1.00
Ne	0.027	0.038	1232	486	0.015	0.22
Mg	0.0070	0.0099	247	323	0.0039	0.12
Si	0.038	0.054	-672	677	0.021	0.12
S	0.020	0.028	-685	787	0.011	0.053
Ar	0.010	0.015	-656	920	0.0056	0.013
Fe_{Si}	0.073	0.10	-486	420	0.041	0.23
Fe_α	0.029	0.041	-1900	-104	0.016	
M_X	2.00	2.84	-210	680		
M_{tot}	2.18	3.14	-210	680		

Note. — Solar abundance ratios from Grevesse et al. (2010). Inferred masses scale as the square root of the filling factor. The Fe masses are taken for a probability threshold 0.01 as discussed in the text and given in Table 3.

Table 3: Fe_{Si}, Fe_{α} Masses

$Fe_{Si,2.5''}$	$Fe_{\alpha,2.5''}$	$Fe_{Si,5''}$	$Fe_{\alpha,5''}$	probability
0.061	0.095	0.086	0.13	10^{0}
0.070	0.049	0.098	0.070	10^{-1}
0.073	0.029	0.10	0.041	10^{-2}
0.075	0.019	0.11	0.027	10^{-3}
0.076	0.012	0.11	0.017	10^{-4}
0.076	0.0092	0.11	0.013	10^{-5}
0.077	0.0063	0.11	0.0089	10^{-6}
0.077	0.0050	0.11	0.0071	10^{-7}
0.077	0.0043	0.11	0.0060	10^{-8}

Note. — Fe masses from incomplete Si-burning (Fe_{Si}) and from complete Si-burning and/or α-rich freeze out (Fe_{α}) in $M_{\odot}$. The final column gives the probability that the second Fe component is not justified by the reduced χ^2 resulting from its inclusion in the fit. Demanding a lower probability reduces Fe_{α}.